A NUMERICAL AND EXPERIMENTAL APPROACH TO IMPLEMENT ACTIVE VIBRATION CONTROL FOR COMPLEX STRUCTURES: A DEMONSTRATION ON A VEHICLE

by

Egemen Aşkın

A Thesis Submitted to the

Graduate School of Engineering

in Partial Fulfillment of the Requirements for

the Degree of

Master of Science

in

Mechanical Engineering

KOÇ
UNIVERSITY

September 2016

Koç University

Graduate School of Sciences and Engineering

This is to certify that I have examined this copy of a master's thesis by

Egemen Aşkın

and have found that it is complete and satisfactory in all respects,
and that any and all revisions required by the final
examining committee have been made.

Committee Members:

Assoc. Prof. Ipek Basdogan

Assist. Prof. Polat Şendur

Assoc. Prof. Murat Sözer

Date: 09.09.2016

ABSTRACT

In recent years, customer requirements for comfortable and quieter vehicles have inspired the automotive manufacturers to introduce new technologies to improve the noise, vibration and harshness (NVH) characteristic for new models. Moreover, the automotive manufacturers need to stay within the weight limits to be competitive in the market while achieving required NVH performance. As an alternative to conventional passive treatments such as mass-damper mechanisms, damping layers and heavy acoustic packages, low weight piezoelectric patches can be easily integrated to vehicle panels to reduce vibrations due to external disturbances actively

Active vibration control (AVC) implementations in the literature are mostly focused on simple geometries with properly defined boundary conditions. However, in real life applications, the structures are much more complex than simple plate and beams. Furthermore, the boundary conditions are not usually well-defined. In this thesis, an active vibration control methodology is developed which incorporates numerical and experimental studies in a structured framework to reduce undesired vibrations of complex systems.

In this thesis, first, the developed methodology is demonstrated on a representative vehicle model in the laboratory environment considering the complex shape, boundary conditions and geometric constraints. Optimum location for the sensor/actuator pair is determined numerically by using a validated finite element model (FEM) of the complex structure. Once the optimum location is determined, the controller parameters (e.g. damping and gain) are varied based on Design of Experiments (DOE) technique to search for the optimum parameter configuration in the design space. All the DOE configurations are performed experimentally to include the hardware and controller limitations in the analysis. Response Surface Methodology (RSM) technique is utilized for identifying the relationship between the design parameters and the controller performance. The vibration suppression performance is evaluated based on two control metrics, the amplitude reduction at the targeted frequency and broadband energy reduction. Single and multi-objective optimization case studies are performed using the above metrics.

Finally, the same approach is extended to a real vehicle with hardware modifications due to power constraints in the operating condition. It was observed that the developed active vibration methodology can be applied effectively to complex systems to reduce the undesired vibrations. Moreover, the methods presented in this thesis can be implemented to other areas such as aerospace and marine applications.

Keywords: Active Vibration Control, PPF Controller, Finite Element Method, Numerical and Experimental Studies, Response Surface Methodology, Multi Objective Optimization, Vehicle Testing, Modal Testing, Complex Structures

ÖZETÇE

Günümüzde müşterilerin daha konforlu ve sessiz araçlar talep etmeleri, otomotiv üreticilerini titreşim, gürültü ve sertlik (NVH) karakteristiğini iyileştirmek adına yeni modellerde ileri teknolojilere yönelmelerini sağlamıştır. Buna ek olarak otomotiv üreticileri, gereken NVH karakteristiğini sağlarken, pazarda rekabetçi konumda bulunabilmek adına ağırlık hedeflerinden de sapmamaları gerekmektedir. Kütle-damper mekanizması, sönümleme pedleri ve ağır akustik paketler gibi geleneksel pasif uygulamaların aksine, düşük ağırlığa sahip piezoelektrik yamalar kolaylıkla araç paneline entegre edilip dış tahriklerden dolayı meydana gelen titreşimleri aktif yöntemlerle sönümleyebilmektedir.

Literatürdeki aktif titreşim kontrolü (AVC) çalışmaları genelde basit geometriye ve elverişli sınır koşullarına sahip panellerde gerçekleştirilmiştir. Fakat gerçek hayatta yapılar, literatürdeki basit plaka ve kirişlere kıyasla oldukça karmaşık geometrilere sahiptir. Ayrıca sınır koşulları da önceden belirlenmiş şekilde elverişli değildir. Bu tezde nümerik ve deneysel çalışmalar birleştirilerek elde edilen aktif titreşim kontolü yöntemiyle, karmaşık sistemler üzerindeki istenmeyen titreşimlerin önlenmesi sağlanmaktadır.

Bu tez kapsamında ilk olarak, geliştirilen yöntem karmaşık geometriye sahip, zorlu sınır koşulları ve geometrik kısıtları olan temsili araç düzeneğinde laboratuvar ortamında gerçekleştirilmiştir. Aktif titreşim kontrolünde kullanılacak sensör/aktüatör çiftlerinin karmaşık yapı üzerindeki ideal lokasyonları, doğrulanmış sonlu elemanlar modeli (FEM) kullanılarak nümerik olarak belirlenmiştir. İdeal olan konumlandırma gerçekleştikten sonra, kontrolcü parametrelerinin (damping ve gain) değerleri deneysel tasarım (DOE) tekniği kullanılarak farklı seviyelerde denenmiş ve ideal kontrolcü parametreleri bulunmuştur. Dizayn parametreleri ile kontrolcü perfromansı arasındaki ilişki Cevap Yüzeyi Yöntemi (RSM) yardımıyla gerçekleştirilmiştir. Bu çalışmadaki titreşim sönümleme performansı iki kriter üzerinden değerlendirilmiştir: hedef frekanstaki titreşim genliği indirgemesi ve geniş frekans bandında enerji azaltımı. Yukarıdaki kriterler temel alınarak tek amaçlı (single objective) ve çok amaçlı (multi-objective) optimizasyonlar gerçekleştirilmiştir.

Son olarak, karmaşık geometriye sahip düzenekte elde edilen çıktılar ve yapılan çalışmalar, araç seyir halindeyken gerekecek ekstra donanımlar ve güç kısıtlamaları üzerine çalışılarak gerçek araç seviyesinde genişletilmiştir. Bu bölümdeki deneylerin sonuçlarına göre, geliştirilen aktif titreşim kontrolü yönteminin karmaşık sistemler üzerindeki istenmeyen titreşimleri etkili bir biçimde indirgeyebildikleri saptanmıştır. Ayrıca, bu tezde sunulan yöntemin uzay ve gemi endüstrisi gibi diğer disiplinlere de uygun olduğu düşünülmektedir.

Anahtar Kelimeler: Active Titreşim Kontrolü, PPF Kontrolcü, Sonlu Elemanlar Yöntemi, Nümerik and Deneysel Çalışmalar, Cevap Yüzeyi Yöntemi, Çok Amaçlı Optimizasyon, Araç Testi, Modal Test, Karmaşık Yapılar

ACKNOWLEDGEMENTS

I would like to thank and express my deepest gratitude to my advisor Assoc. Prof. Dr. İpek Başdoğan for giving me the chance to be a member of Vibration and Acoustics Laboratory at Koç Unviersity, providing invaluable guidance, and granting us a productive environment and well equipped laboratory. I appreciate all her support and contributions which encourage us to research.

Besides my advisor, I would like to thank my thesis committee: Assist. Prof. Dr. Polat Şendur and Assoc. Prof. Dr. Murat Sözer for their thorough review of my work and showing delicacy to attend my thesis defense.

I am grateful to thank my company Ford Otosan in supporting employees for graduate studies and providing opportunities for me to use their facilities and equipment. I am also grateful to Dr. Yüksel Gür from Ford Motor Company Advanced Research Center for sharing his expert knowledge and creative thinking.

I am very thankful to all my good friends and lab mates Utku Boz, Hakan Yenerer, Buğra Bayık, Uğur Arıdoğan, Gökhan Serhat, Mehmet Murat Gözüm, and Amirreza Aghakhani for providing very friendly and insightful discussions to proceed in my research.

Last but not least, I thank my wife for her love, support and patience in every step of my life.

TABLE OF CONTENTS

LIST OF FIGURES

LIST OF TABLES

Chapter 1

INTRODUCTION

1.1. Review of Active Vibration Control Applications in the Literature

In recent years, customer requirements for comfortable and quieter vehicles have inspired the automotive manufacturers to introduce new technologies to improve the noise, vibration and harshness (NVH) characteristic for new models. Moreover, the automotive manufacturers need to stay within the weight limits to be competitive in the market while achieving required NVH performance.

Conventional applications of vibration treatments today need compromise between weight and performance since sometimes increasing vibration performance requires adding considerable weight to the system. An effective alternative that overcomes the drawbacks of passive applications is the utilization of piezoelectric materials in active vibration control.

Active vibration control implementations in the literature are mostly focused on simple geometries with properly defined boundary conditions. However, in real life applications, the structures are much more complex than simple plate and beams. Furthermore, the boundary conditions are not usually well-defined.

In low frequency vibrations, passive isolation methods generally fail and it is not always feasible to use structural modification techniques as the complexity of the design increases. For those cases, active vibration control technique is an effective alternative. The active vibration control applications received attention by the researchers in the last two decades.

For instance, Alkhatib and Golnaraghi [1] reviewed the structural control strategies and summarized general design procedures for the AVC systems. Among the few pioneering studies, Ro and Baz [2], investigated the performance of active and passive layers for low frequency vibrations and stated that derivative control provides higher damping ratios compared to the passive damping treatments.

With the development of the smart materials, piezoelectric materials have been employed as sensors and actuators in vibration and noise control systems. Bailey and Hubbard [3], studied an active damper system using piezoelectric materials distributed over the surface of a cantilever beam and increased the modal loss factor from 0.003 to 0.04. In addition to those initial studies, other authors showed the efficiency of active vibration controllers utilizing piezoelectric materials for low frequency vibrations. Among the recent studies, Boz et al. [4] demonstrated the efficiency of AVC on a fully clamped plate by employing optimal velocity feedback control. Furthermore, Li et al [5], developed a dynamic observer controller combining LQR algorithm with feed-forward compensation to suppress vibration of a fully clamped plate using piezoelectric actuators and avoid spillover.

In active vibration control applications, various types of controller architectures are used. In this study, Positive Position Feedback (PPF) algorithm, proposed by Caughey and Goh [6] is used to actively control a complex structure. Among various alternatives, PPF is one of the most useful techniques because of its stability and ease of implementation [7]. Caughey and Fanson [8] showed that PPF is able to control first six bending modes in large space structures with modal damping as high as 20%.

As in the all control architectures available for AVC, the effectiveness of the PPF controller strongly depends on the piezoelectric sensor and actuator positions on the host structure. In one of the preliminary works, Crawley and DeLouis [9] placed the surface bonded actuator at the maximum strain location at a specific mode of an aluminum beam for single mode vibration. However, the placement problem for two or more target frequencies was not addressed. Optimal sensor/actuator placement for plate structures were also studied in [10], [11]. Detailed information on effective sensor/ actuator location was investigated and reviewed by Gupta et. al [12]. They reviewed the optimal positioning of the sensor/actuator pairs on cantilever beams and plates based on maximizing modal forces and moments, minimizing control effort, minimizing spill-over effects and maximizing degree of controllability. Liu and Hu [13] introduced a model correlation criterion and used controllability and observability Grammians as the sensor/actuator placement optimization criteria. They were able to suppress the vibrations of a spacecraft structure with fewer actuator and sensors for multi-modal suppression by optimizing sensor/actuator placement. All of the above studies indicated that optimal placement of the piezo actuators was crucial for vibration suppression; however demonstration of the developed methods were limited to simple beam or plate like structures with well-defined boundary conditions.

Once the best sensor/actuator location is determined, the controller parameters must be optimized to improve the controller performance. Goh and Lee [14] stated that effective vibration control by utilizing PPF highly depends on structural damping ratios and frequencies. Goh and Caughey [6] utilized a pole placement approach to calculate damping, gain and frequency which assures maximum closed loop reduction. Ryan and Jinjun [15], utilized a PPF controller to reduce vibrations occurring on a one-link manipulator. The genetic algorithm (GA) was used to optimize all controller parameters of a collocated piezoelectric sensor/actuator pair by minimization of the closed loop H_∞ norm. In another study, McEver [16] specified that the optimal parameters can be extracted from the ratio of structural zero frequencies to the structural poles. Considering the difficulties encountered in designing a controller as described in the previous studies, a numerical and experimental methodology is developed in this thesis to implement AVC for complex structures.

First the developed methodology is demonstrated on a representative vehicle model in the laboratory environment considering the complex shape, boundary conditions and geometric constraints. Optimum location for the sensor/actuator pair is determined numerically by using a validated finite element model of the complex structure. Once the location is determined, the controller parameters (e.g. damping and gain) are varied based on Design of Experiments (DOE) technique to search for the optimum parameter configuration in the design space. All the DOE configurations are performed experimentally to include the hardware and controller limitations in the analysis. RSM technique is utilized for identifying the relationship between the design parameters and the controller performance. Then, vibration suppression performance is evaluated based on two control metrics, amplitude reduction at the targeted frequency and broadband energy reduction. Single and multi-objective optimization case studies are performed using the above metrics. Finally, the same approach is extended to a real vehicle with hardware modifications due to the power constraints in the operating conditions. It was observed that the developed active vibration methodology can be applied effectively to complex systems to reduce the undesired vibrations.

1.2. Contribution of This Thesis

In this thesis, a numerical and experimental methodology is developed to implement AVC for complex structures. The methodology is first implemented on a complex vehicle structure in the laboratory environment, then, on a vehicle running in real operating conditions. The major contributions of this thesis can be summarized as follows:

- Development of complex, detailed and high fidelity FE model representing experimental structure characteristics.
- Verification of the FE model in terms of frequency, mode shapes and frequency response functions (FRF) correlation

- Integration of the piezoelectric patches to the numerical model and determine optimized location of sensor/actuator pair
- Optimization of the PPF controller parameters by using DOE and RSM techniques based on two performance metrics: amplitude reduction at target frequency, broadband energy reduction in terms of H_2 norm
- Experimental verification of the optimal controller settings
- Implementation of the AVC system on a vehicle in real operating conditions.

1.3. Thesis Layout

In Chapter 2, experimental structure and FE model are introduced. The details of the modal test of the experimental structure are presented and modal test and modal analysis results are shown. FE model is verified by comparing the experimental and numerical models results in terms of frequency, FRFs and mode shapes.

In Chapter 3, the details of the piezoelectric material model are introduced. Integration of piezoelectric patches to the FE model is presented. The proposed methodology for optimal placement of piezoelectric sensor/actuators is given in detail. The results for various locations are analyzed and the optimum location is determined.

In Chapter 4, the details of the methodologies for optimizing the PPF controller parameters are introduced. Single and multi-objective optimization studies are performed using two performance metrics: amplitude reduction at the targeted frequency and broadband energy reduction in terms of H_2 norm. Effect of damping and gain on each performance metric is illustrated. Then optimal configuration of gain and damping values are verified experimentally.

In Chapter 5, optimized PPF controller configuration is implemented on a real commercial vehicle. Hardware modifications and power constraints for implementing the developed approach is presented in detail. Experimental conditions and vehicle test scenario are described in detail. Vehicle level AVC results are introduced.

Finally in Chapter 6, main conclusions and future work recommendations are summarized.

Chapter 2

EXPERIMENTAL STRUCTURE, FEM AND VALIDATION WITH MODAL TEST

2.1. Overview

In this chapter, the experimental structure which is a representative vehicle model is introduced. This structure is utilized for determining the optimal piezoelectric sensor/actuator position and PPF controller parameters. A high fidelity FEM is used to determine the optimal positions on the structure for the sensor/actuator pair. This chapter summarizes element and connection types and boundary conditions of the FEM

In this chapter, modal test of the experimental structure are also given. Experimental natural frequencies and mode shapes are compared with the FE model predictions to validate the model.

2.2. Experimental Structure

A representative vehicle model is built in the laboratory environment. It is the one quarter of a vehicle Body in White (BIW) assembly which includes the wheelhouse. The wheelhouse region was selected for AVC studies. It is known that road induced excessive vibrations occur on the wheelhouse during the cruise condition due to the close location to the wheels. A support system is designed and manufactured to locate the quarter BIW assembly to ensure stability and also simulate the real boundary conditions. The final assembly is illustrated in Figure 1.

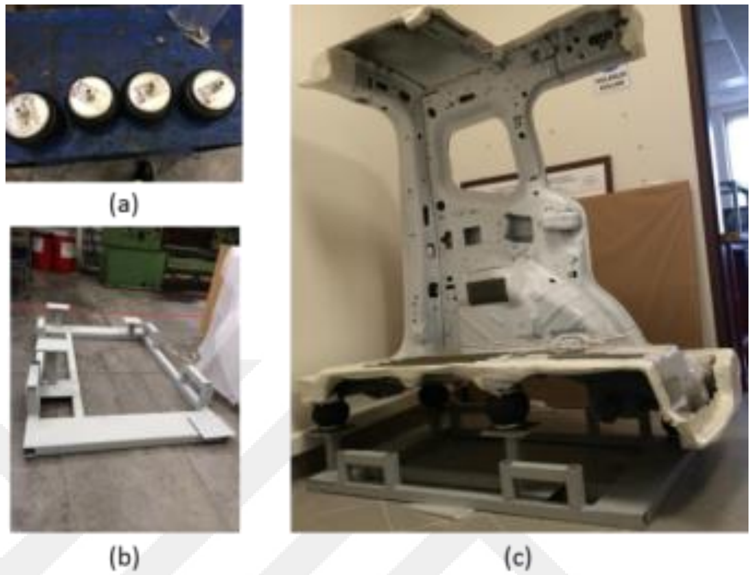

Figure 1 Details of the Quarter BIW assembly a) Air Mounts b) Skid c) Overall assembly

2.3. Finite Element Model of Experimental Structure

FE model is utilized for modelling piezoelectric patches and the experimental structure. The FEM of the experimental structure here is shown in Figure 2. ABAQUS is used to generate FEM of the structure panels, spot welds, adhesive layers and piezoelectric elements with its bonding to the wheelhouse panel. The FE model consists of nearly 100,000 nodes and hence the degree of freedom is 600,000.

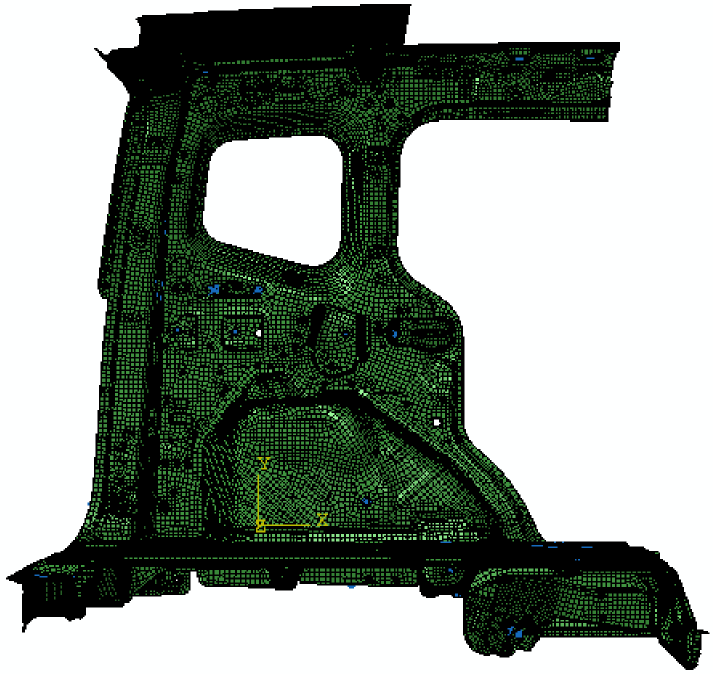

Figure 2 Finite Element Model of the Experimental Structure

In FE model, sheet metals are modeled as Shell elements (S3R and S4R) since this is the best way to model curved, intersecting shells that exhibit general purpose [17]. Spot welds are modeled with shell to solid constraints and used to connect the panels. In spot weld modelling, solid (hexahedra) element represents the spot weld and two tie constraints (if it is a 2T connection) simulates the bonding of opposing panels to the spot weld. With this approach, we assure the displacement of the shell node at one panel is strongly bonded, as strong as steel, to a shell node of the corresponding panel through the reciprocal edges. Solid element is modeled with a steel property. Material properties of spot weld materials are listed in Table 1. In this model, the spot welds connect maximum of 3 panel. Except spot weld, there are other connections as adhesive lines and bolt joints. Adhesive lines also utilize solid elements like spot welds but with weaker material properties since they are mastics. Unlike spot welds, adhesive connections are lines of solid elements with the same tie constraints. Adhesive connection material properties are listed in Table 1. Bolt models are composed of ABAQUS multi-point constraints (MPC) elements by selecting all nodes on two reciprocal panel holes. Since MPC is a rigid constraint, no material property is defined in this case.

Table 1 Properties of the Experimental Structure and FE Model

	Assembly	***Wheelhouse Panel***	***PZT Patch***
Material(s)	Steel$_1$, Soft Seal$_2$, Roof Adhesive$_3$, Structural Adhesives$_4$	Steel	Lead-Zirconate-Titanate
Depth (mm)	840	170	65
Width (mm)	1400	810	31
Height (mm)	1490	440	0.5
Thickness (mm)	0.7 - 3	0.7	0.5
Elastic Modulus (MPa)	210000$_1$, 1.5$_2$,2.26$_3$,1500$_4$	210000	70200
Poisson's Ratio	0.33$_1$, 0.45$_2$,0.42$_3$ 0.37$_4$	0.33	0.36
Density (kg/m^3)	7850$_1$, 9$_2$, 28$_3$, 1380$_4$	7850	7600
Weight (kg)	70.5	2.1	0.0028
Piezoelectric Strain Constant d_{31} (10^{-10} m/V)	-	-	1.74
Piezoelectric Strain Constant d_{33} (10^{-10} m/V)	-	-	3.94
Piezoelectric Strain Constant d_{51} (10^{-10} m/V)	-	-	5.35

2.4. Modal Test and Analysis

The purpose of the modal test is to determine the modal parameters of the structure as resonance frequencies (ω_k), mode shapes and modal damping (c_k). Modal parameters represent the dynamic characteristics of the structure and enable extracting modal behavior. Modal parameters are obtained by post processing frequency response functions (FRF).

In this study, we performed modal test on the wheelhouse panel which is divided into 74 measurement points and 7 zones as indicated in Figure 3. Rowing accelerometer technique is utilized and maximum frequency is selected as 312.5 Hz. Up to maximum frequency, 401 data were collected therefore the frequency resolution is 0.78 Hz. The measurements obtained from the structure are averaged 3 times to construct FRF. Experimental structure has 16 modes for the selected frequency range but first five modes are considered since 0-200 Hz is the concern of this study. Zone 1 is found to be the most influential sub region by observing the high strain regions.

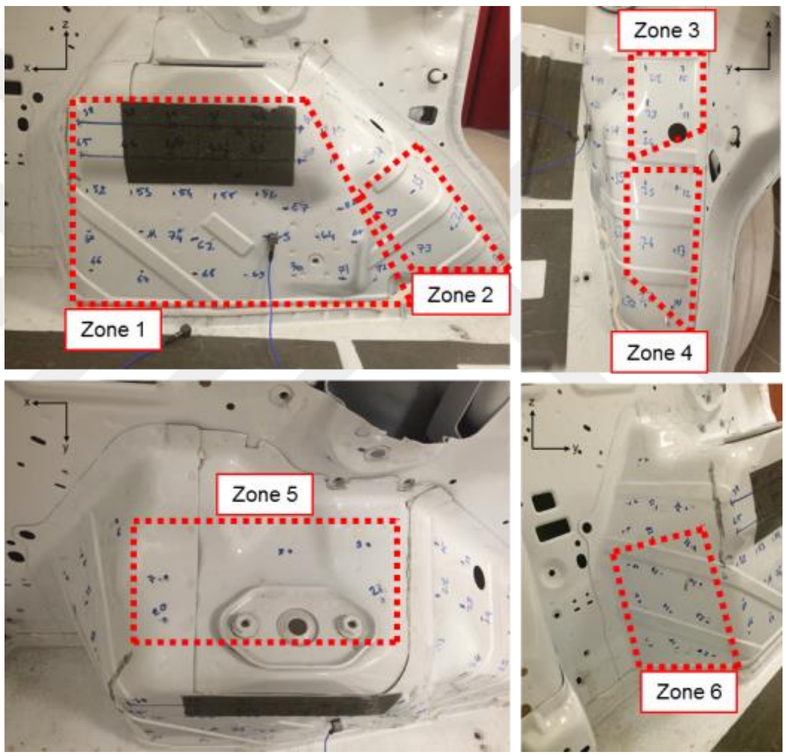

Figure 3 Experimental Structure Sub-regions for Modal Test

All points inside Zone 1 of the experimental structure are indicated in FEM and FRFs are collected numerically. In ABAQUS, performing modal analysis and generating FRFs are two different steps. In the first step, modal analysis is performed by setting the procedure to "Linear perturbation", and select frequency. The resonance frequencies and mode shapes are calculated in the first step. In the second step, steady state dynamics analysis is performed to obtain transfer function (FRF) between two nodes. Figures 4 and 5 show the natural frequencies and the mode shape of the experimental and numerical models, respectively.

Figure 4, experimental modal damping values are also demonstrated. In the next section, detailed comparison of those values and correlation results will be given.

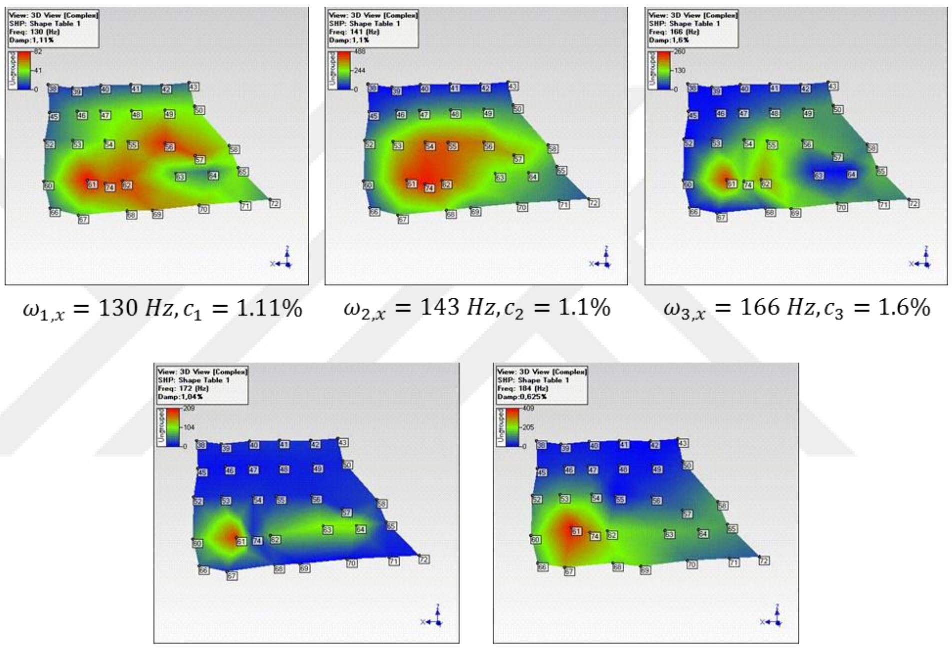

$\omega_{1,x} = 130\ Hz, c_1 = 1.11\%$ $\omega_{2,x} = 143\ Hz, c_2 = 1.1\%$ $\omega_{3,x} = 166\ Hz, c_3 = 1.6\%$

$\omega_{4,x} = 172\ Hz, c_4 = 1.04\%$ $\omega_{5,x} = 184\ Hz, c_5 = 0.625\%$

Figure 4 Experimental Modal Test Results of First 5 Modes

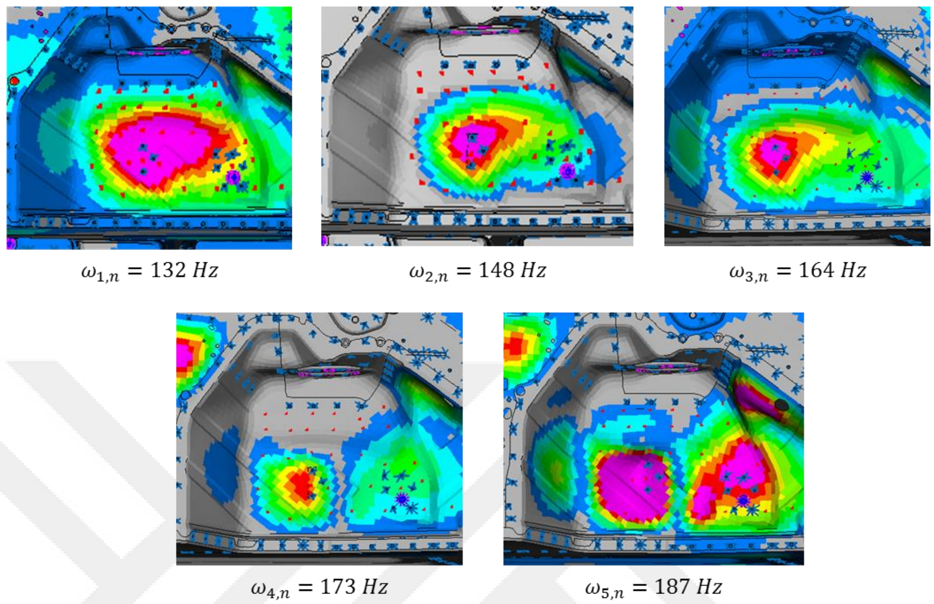

Figure 5 Modal Analysis Results of First 5 Modes

2.5. Correlation

The first step to validate numerical models is to make a direct and objective comparison of specific dynamic properties [18]. The second step is the correlation which enables to specify the differences between experimental and numerical models. If the model is highly correlated, then we can state that the numerical model properly represents the experimental model. And the third step is defined as the correction of the numerical model by considering the differences determined in the second step. The last two steps are known as model updating [18]. In model updating, first the models are compared which enables evaluation of the capability of the numerical model and to see the improvement when the model is updated. Verification of experimental and numerical models is divided into two groups. The first group includes graphical mode shapes comparison and FRF comparison. The second group consists of mathematical formulations such as Modal Assurance Criteria (MAC).

2.5.1 Verification by Frequency Comparison

The fundamental verification method for numerical models is comparison of natural frequencies with the ones obtained via experimental modal analysis. Differences between frequencies indicate the capability of numerical model for each mode. **Table 2** lists the natural frequency values of experimental and numerical models. From the table, it is observed that first five modes contain 1.6%, 3.4%, 1.2%, 0.5% and 1.6% errors, respectively. Calculated errors of first five modes point out that the numerical model is highly correlated in terms of natural frequencies.

Table 2 Experimental and Numerical Natural Frequencies

Result	Mode 1	Mode 2	Mode 3	Mode 4	Mode 5
Experimental	*130 Hz*	*143 Hz*	*166 Hz*	*172 Hz*	*184 Hz*
Numerical	*132 Hz*	*148 Hz*	*164 Hz*	*173 Hz*	*187 Hz*

2.5.2 Verification by FRF Data Comparison

Location of the peaks which represent the natural frequency information of structures is insufficient to verify the numerical model. For FRF comparison, experimental and numerical transfer functions between two points are compared to see the correlation. Amplitudes of those peaks should also be close to experimental results for verification and it is enabled by adjusting modal damping values using the modal test data. The damping values of the experimental model are indicated in Figure 4. If the damping values cannot be obtained from the experimental data, there could be discrepancies between the experimental and numerical results [18]. Figure 6, Figure 7 and Figure 8 illustrate comparison of experimental and numerical FRF's for the same input point "71" to 3 different output points: "38, 61 and 74", respectively. Below plots indicate that, there is a good correlation between the numerical and experimental results.

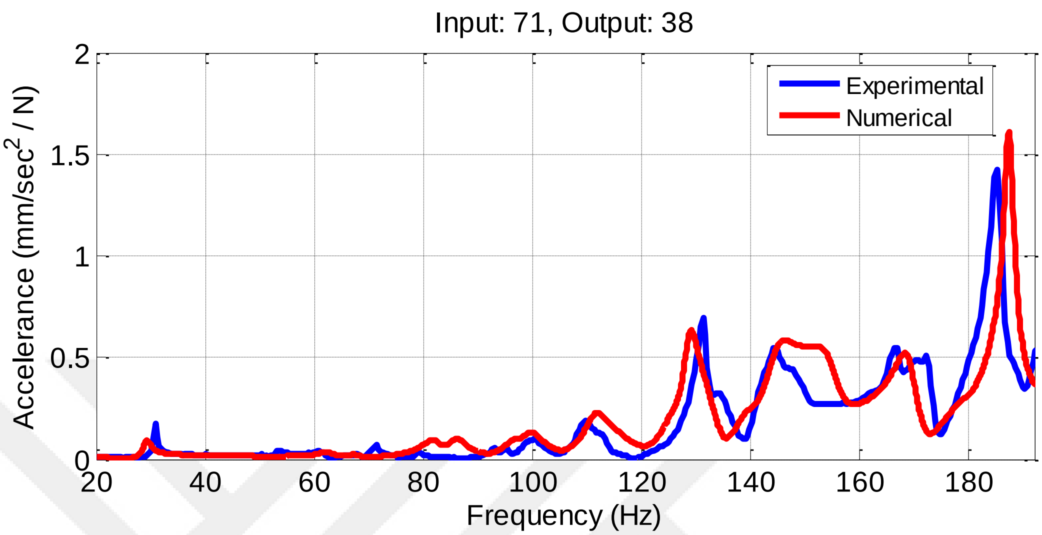

Figure 6 FRF Comparison of Experimental vs Numerical. Input: 71, Output: 38

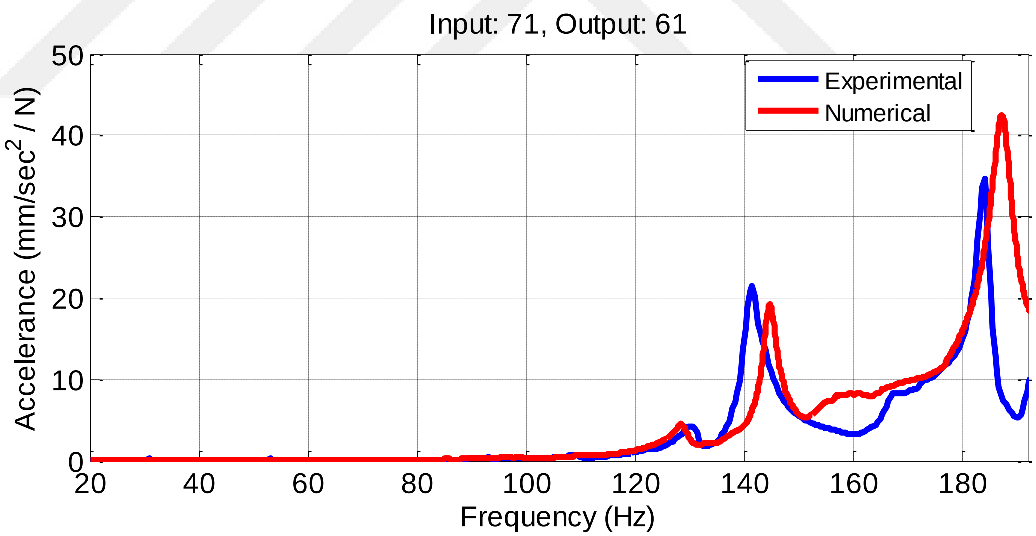

Figure 7 FRF Comparison of Experimental vs Numerical. Input: 71, Output: 61

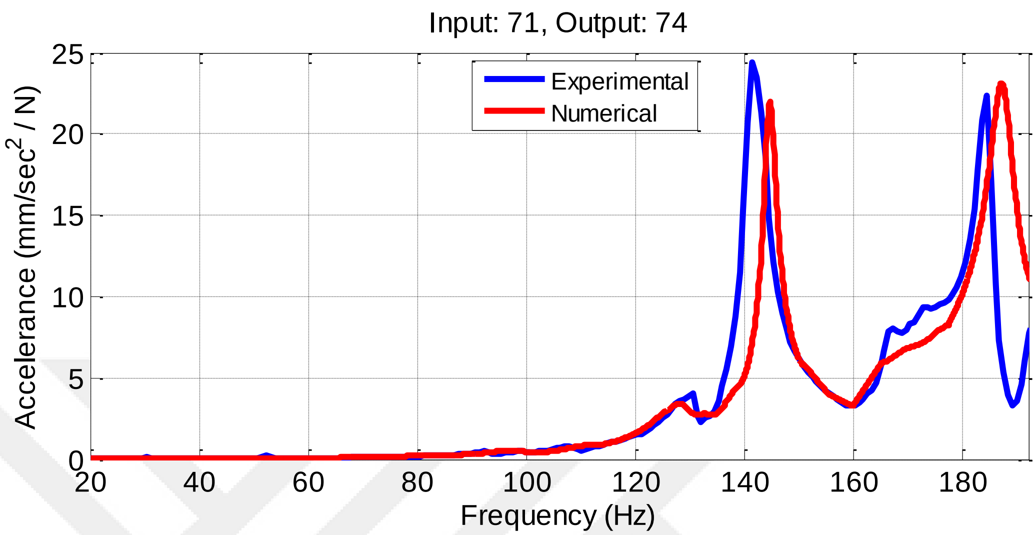

Figure 8 FRF Comparison of Experimental vs Numerical. Input: 71, Output: 74

2.5.3 Verification by Mode Shapes Comparison

Comparison of mode shapes are performed in two ways: graphical comparison and comparison with mathematical methods. Graphical comparison should be utilized through examining animations of experimental and numerical mode shapes. This approach provides limited information about the structure since this is visual. In this study, graphical comparison of experimental and numerical mode shapes could be performed by examining Figure 4 and Figure 5.

Comparison of mode shapes by mathematical methods is usually performed by Modal Assurance Criteria (MAC). This parameter provides a measure of the least squares deviation or scatter of the points from the straight line correlation and is useful to quantify the degree of correlation between two sets of mode shape data [18]. MAC is defined by:

$$MAC(A,X) = \frac{(\{\Psi\}_A^T\{\Psi\}_A)^2}{(\{\Psi\}_A^T\{\Psi\}_A).(\{\Psi\}_X^T\{\Psi\}_X)} \tag{1}$$

where $\{\Psi\}_X$ is experimentally measured mode shape and $\{\Psi\}_A$ is numerical mode shape. From this calculation one should expect that when experimental and numerical mode shapes used are the same mode, then the MAC value is close to 1.0, whereas if two modes are completely different, then MAC value is close to 0.0. Consider a MAC analysis for 5 modes. For each experimental and numerical mode shapes 5 x 5 MAC matrix is created to indicate which experimental mode relates to which predicted one. MAC table performed for this study is shown in Figure 9.

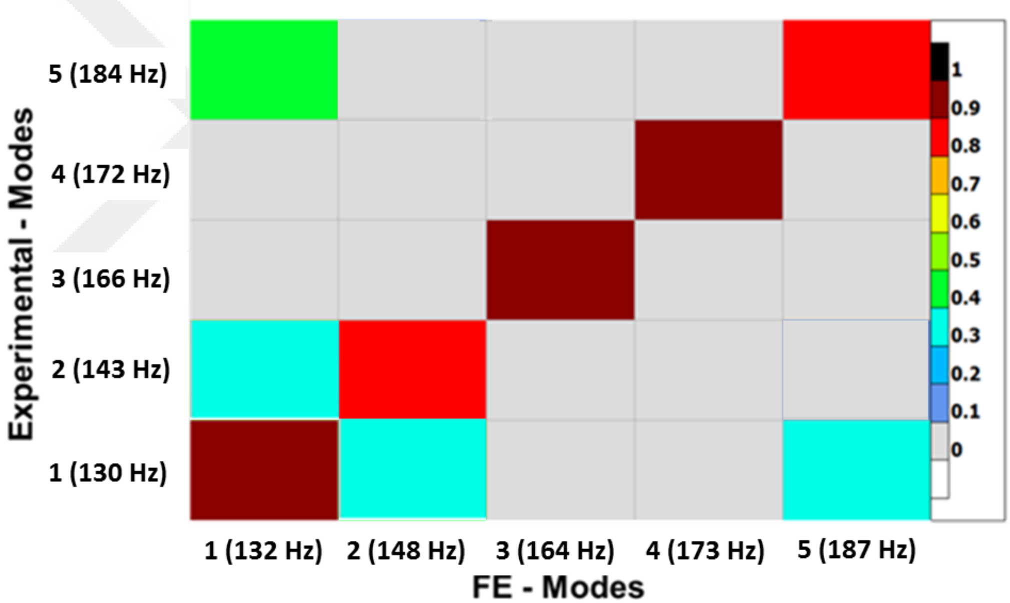

Figure 9 MAC Plot for Mode Shapes Correlation

In this plot, diagonal values which exceed 0.8 is considered as well correlated modes and values of less than 0.2 as uncorrelated modes. There are some reasons why MAC values may be less than unity besides obvious incorrect models which are non-linarites in the test structure, noise on the measured data, poor modal analysis of the measured data and inappropriate choice of DOFs included in the correlation [18]. In this study, MAC values for the first five modes are above 0.8. Grey regions indicate no correlation for the specified regions. However there are some regions other than red or grey which exhibit small correlation such as between numerical mode shape 2 and experimental mode shape 1, numerical mode shape 1 and experimental mode shape 2, numerical mode shape 1 and experimental mode shape 5, and finally numerical mode shape 5 and experimental mode shape 1. The values at those regions indicate that different mode shapes are similar with small correlation.

Chapter 3

OPTIMAL PLACEMENT OF PIEZOELECTRIC ACTUATORS AND SENSORS

3.1. Overview

The placement of piezoelectric actuators and sensors has a significant impact on the vibration suppression performance [19]. In control applications, it is advantageous to select a collocated configuration for the sensor/actuator pairs. However, in this case it is not possible to place the actuator and the sensor at the collocated location on the wheelhouse since outer surface corresponds to the exterior of the vehicle. It is not feasible to place the piezoelectric patches at the outer surface because of the environmental effects such as vulnerability of piezoelectric patches to dust and rain.

In order to achieve best performing sensor/actuator location, all the possible configurations were considered to investigate the effectiveness of the sensor/actuator locations. Optimum location investigations are carried out using the FEM. The FEM details of the representative vehicle model are provided in the previous section and integration of the piezoelectric patches to the FE model will be described in this section

3.2. Finite Element Modelling of Piezoelectric Patches

Finite element methods have been developed for piezoelectric beams based on the linear theory of piezoelectricity. The piezoelectric elements include axial, transverse, rotational and electrical degrees of freedom. In this thesis, piezoelectric layers were generated using the piezoelectric modeling capabilities of ABAQUS, with twenty-node, three-dimensional continuum piezoelectric elements (C3D20RE).

In the modelling of structures with embedded piezoelectric active devices, three kinds of finite elements are required as three-dimensional finite elements which can couple the elastic and electric fields, shell finite elements for the plate structure, and transition elements. In this study, one solid piezoelectric element is used for piezoelectric patch and one solid element is used for modelling the adhesive. The FE model of the piezoelectric patch is shown in Figure 10, b and the mechanical properties of piezoelectric patch are illustrated in Table 1.

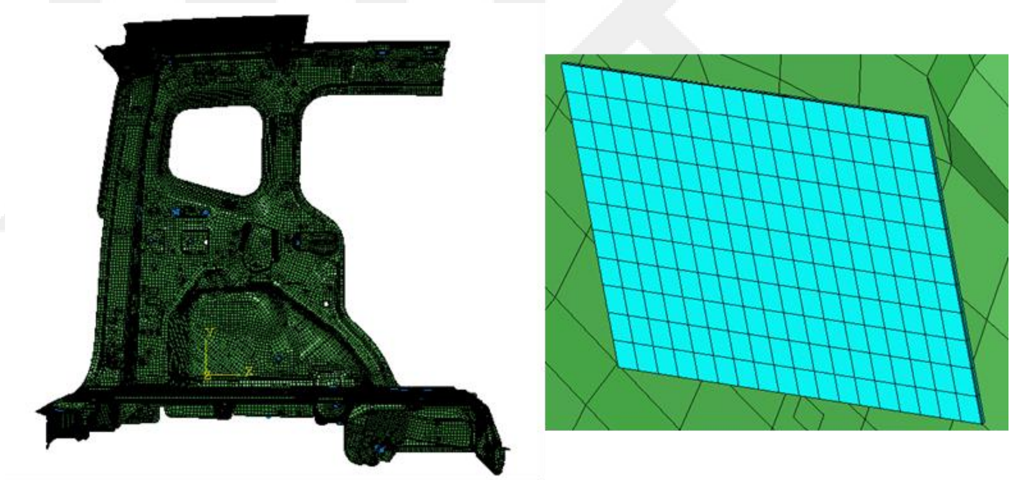

(a) (b)

Figure 10 FE Model of a) Experimental Structure b) Piezoelectric Patches

Piezoelectric materials are anisotropic and the elastic field in such materials is coupled with the electric field. Finite element equations of a piezoelectric actuator embedded on a structure has already been formulated in many papers [20-22]. In this paper, only the results are summarized. The mechanical behavior can be defined by [17]:

$$\sigma_{ij} = D^{E}_{ijkl}\varepsilon_{kl} - e^{\varphi}_{mij}E_m \tag{1}$$

In terms of the piezoelectric stress coefficient matrix, e^{φ}_{mij}. Or

$$\sigma_{ij} = D^{E}_{ijkl}(\varepsilon_{kl} - d^{\varphi}_{mkl}E_m) \tag{2}$$

In terms of the piezoelectric strain coefficient matrix, d^{φ}_{mkl}. The electrical behavior is defined by

$$q_i = e^{\varphi}_{ijk}\varepsilon_{jk} + D^{\varphi(\varepsilon)}_{ij}E_j \tag{3}$$

where σ_{ij} is the mechanical stress tensor,

ε_{ij} is a small strain component,

q_i is electric displacement vector,

D^{E}_{ijkl} is the material's elastic stiffness matrix defined at zero electrical potential gradient

e^{φ}_{mij} is the material's piezoelectric stress coefficient matrix caused by the electrical potential gradient

d^{φ}_{mkl} is the material's piezoelectric strain coefficient matrix caused by the electrical potential gradient

e^{φ}_{ijk} is the piezoelectric stress coupling

φ is the electrical potential,

$D^{\varphi(\varepsilon)}_{ij}$ is the material's dielectric matrix for a fully constrained material, and

E_i is the gradient of the electrical potential along the *i*th material direction, $-\partial\varphi/\partial x_i$.

The material's electrical and electro-mechanical coupling behaviors are defined by its dielectric property, $D^{\varphi(\varepsilon)}_{ij}$ and its piezoelectric strain coefficient matrix, d^{φ}_{mkl}. Therefore, 19 components must be given in the following order:

$$\begin{bmatrix} d^{\varphi}_{1\,11} & d^{\varphi}_{1\,22} & d^{\varphi}_{1\,33} & d^{\varphi}_{1\,12} & d^{\varphi}_{1\,13} & d^{\varphi}_{1\,23} \\ d^{\varphi}_{2\,11} & d^{\varphi}_{2\,22} & d^{\varphi}_{2\,33} & d^{\varphi}_{2\,12} & d^{\varphi}_{2\,13} & d^{\varphi}_{2\,23} \\ d^{\varphi}_{3\,11} & d^{\varphi}_{3\,22} & d^{\varphi}_{3\,33} & d^{\varphi}_{3\,12} & d^{\varphi}_{3\,13} & d^{\varphi}_{3\,23} \end{bmatrix} \quad (4)$$

The piezoelectric materials are deformed under the effect of electrical or physical loads. For actuation or sensing purposes, the piezoelectric materials are bonded to the host structure. Piezoelectric coefficients applied herein are utilized with double subscripts which link electrical and mechanical quantities. The first subscript gives the direction of the electrical field associated with the voltage applied or the charge or the voltage produced. The second subscript gives the direction of mechanical stress or the strain. When electrical charge is applied, piezoelectric materials change volume and generate forces on the bonding surface which eventually cause strain on the host structure.

Piezoelectric patches are modeled as two separate blocks, which are connected at the ground plane. One block is for modeling the active Lead Ziconate Titanate (PZT) piezoelectric material and another block is used as a non-active insulation layer between the host structure and the patch. The active piezoelectric layer is 2 mm and insulation layer is 3 mm. Patch dimensions for both sensor and actuator is 61 x 35 x 5 mm. In this study, commercially available piezoelectric actuator patch (PI Dura-act 876.A12) is used. Technical information about both material properties of active piezoelectric material and the patch connections including the electrical and insulation layer are supplied from the PZT patch manufacturer.

In numerical analyses, sensor patch is positioned at the highest strain region, as in Figure 11, and the electrical charge is applied to the actuator patch with provided electrical limitations by the manufacturer. The patches can operate between (+400, -250) voltage range and this is taken into consideration for simulations by selecting charge amplitude as 0.001. The FRF between actuator patch and sensor patch is measured. The simulated frequency response is obtained between the applied voltage at the actuator patch and output voltage at the sensor patch. To obtain transfer functions between applied voltage and output voltage, for each frequency between 100 Hz to 220 Hz, unit charge is applied to piezoelectric patches with resolution of 1 Hz. Steady state dynamics, direct solver is utilized from the ABAQUS solver options. The resolution of 1 Hz and frequency range of 100-220 Hz are selected due to increased simulation time since each step takes 12 minutes which makes 1400 minutes in selected range with quad core personal computer.

3.3. Sensor/Actuator Configuration Plan

To investigate the optimal sensor/actuator location, the piezoelectric patches were placed on 8 different locations in simulation runs. For each location of the piezoelectric patch, four different orientation angles (e.g. 0°, 45°, 90°, and 135°) are investigated through simulations (See Figure 11). Some orientations and positions are not feasible due to physical constraints of this complex panel such as lack of flat surfaces for bonding PI P876.A12 bender type piezoelectric patches, interference with the beads on the surface, and mode shape of the wheelhouse panel. As a result, predetermined locations entitled as L1, L5, L6 and L7; and O3 orientation at L2 and L3 locations are not suitable to perform the simulations.

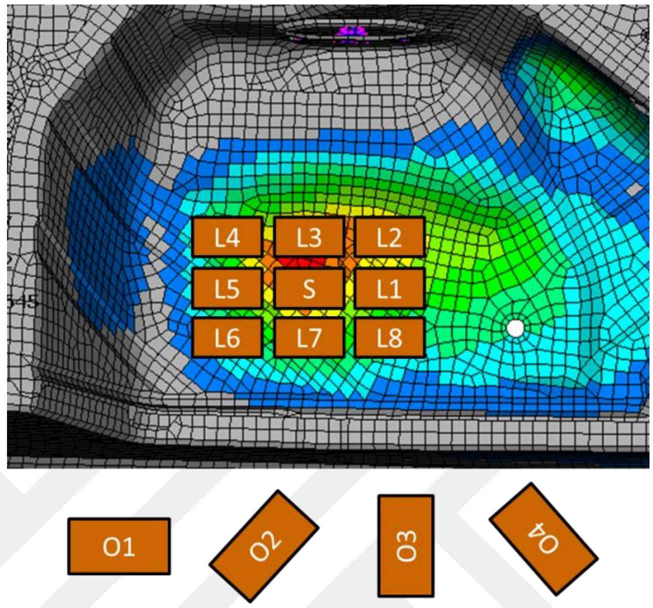

Figure 11 Optimal Positioning Strategy of the Piezoelectric Patches. Locations are above and Orientations are illustrated below

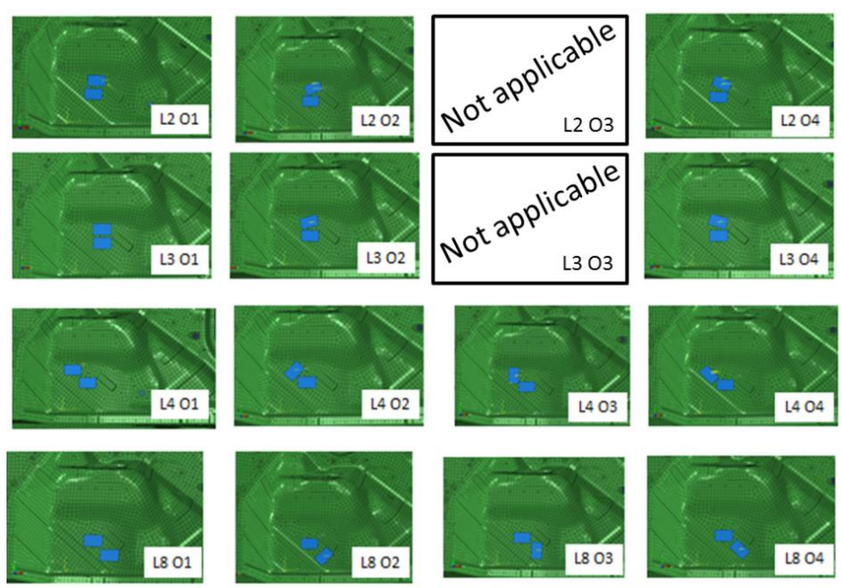

Figure 12 All Possible Configurations in Optimal Positioning

3.4. Location Results

All of the 14 feasible configurations are simulated and the frequency response function at each configuration is obtained by dividing the voltage measured at the sensor patch to the applied voltage at the actuator patch. Figure 13 shows the transfer function response between actuator patch and sensor patch in terms of V/V. Then the best location is determined by selecting the sensor/actuator pair that gives the highest frequency response function at the frequency of interest.

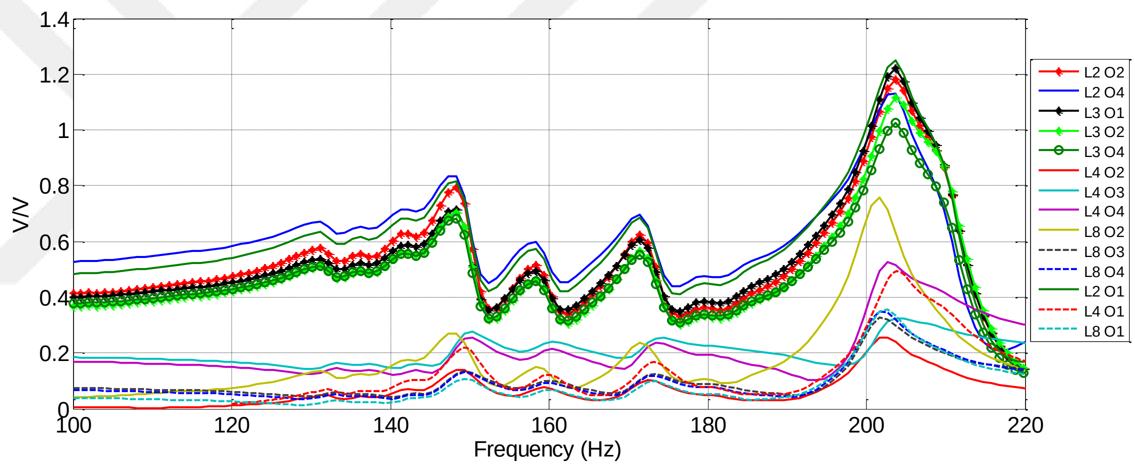

Figure 13 Numerical Results of the Piezoelectric Patches for Optimal Positioning

Based on the evaluations of Figure 13, the optimal locations for the PZT actuator and sensors are determined as shown in Figure 14, which was named as L2 O4.

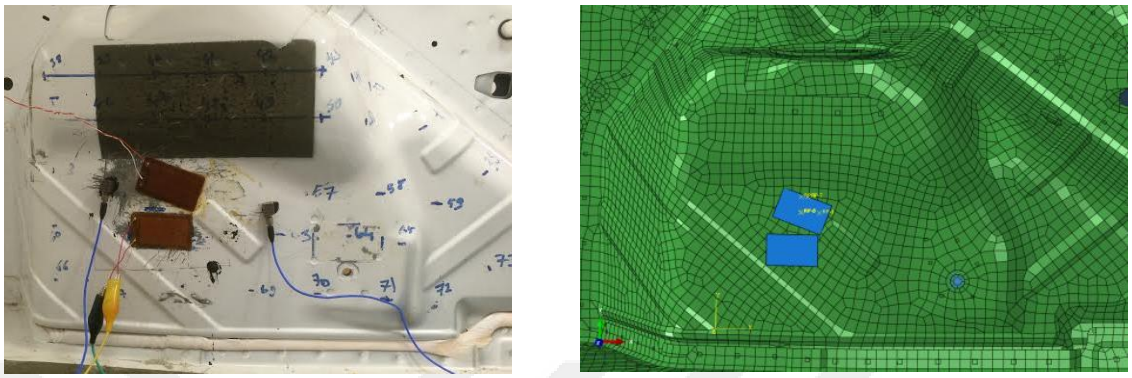

Figure 14 Piezoelectric Patch Locations on the Structure. Experimental Setup on the Left and FEM on the Right

Chapter 4

OPTIMIZATON OF PPF CONTROLLER PARAMETERS

4.1. Overview

Once the optimal position of actuator and sensor couples is determined numerically, next step is to optimize the PPF controller parameters: damping and gain. To achieve this, firstly the system configuration and controller implementation is presented. Then, DOE method and optimization approach is explained. The theoretical background of RSM and steps to construct an experiment plan for this study are also presented in this section.

In section 4.5, finding optimal damping and gain values from experimental RSM based on vibration suppression at the target frequency, broadband energy reduction (H_2 norm), and multi-objective for both cases are shown. Statistical analysis results, surface plots and effect of parameters for each objective are discussed. For the multi-objective optimization part, weighted sum and D-optimality approaches are utilized and it is shown that both approaches output the same optimal results. In the last section of this chapter, optimization outputs are verified experimentally and the results are illustrated in Table 8.

4.2. System Configuration

In this section, the details of the experimental setup used to verify the proposed methodology is shown. The system is composed of the rear left quarter of the vehicle, PZT actuators and sensors, digital controller, signal generator, signal analyzer and PC. Details of the experimental set-up and the components are shown in Figure 15. The PI-P876.A12 type

PZT patches are used as actuators and sensors. Properties of the quarter vehicle structure and the PZT actuators are summarized in **Table 1**.

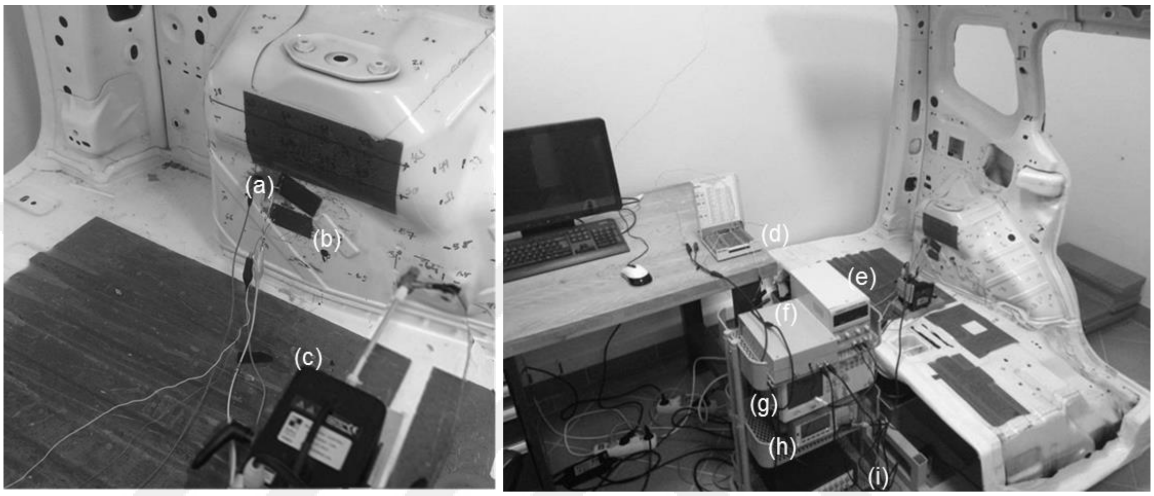

Figure 15 Details of the experimental set-up a) PZT actuator b) PZT sensor c) Shaker d) Controller Unit e) DC Power Supply f) PZT amplifier g) Oscilloscope h) Signal Generator i) Signal Analyzer

4.3. Controller Implementation

The diagram of the controller architecture is shown in Figure 16. The sinusoidal input on the structure is generated using a signal generator and a shaker. The control actuator is used to suppress the vibration of the structure and the sensor is used to evaluate the performance. In addition to the sensor/actuator patch pair, two accelerometers are attached on the structure to monitor the vibration at other locations of the panel and therefore showing the overall effectiveness of the controller. NI-PCI 6229 DAQ unit is used for the controller implementation and the performance of the controller is monitored utilizing a signal analyzer. The control signal is transferred to the control actuator utilizing the

E413.D2 type signal amplifier. The sensor signal and shaker output signals are then transferred to a signal analyzer unit to collect the sensor data. The PPF performance is evaluated by comparing open loop and closed loop data.

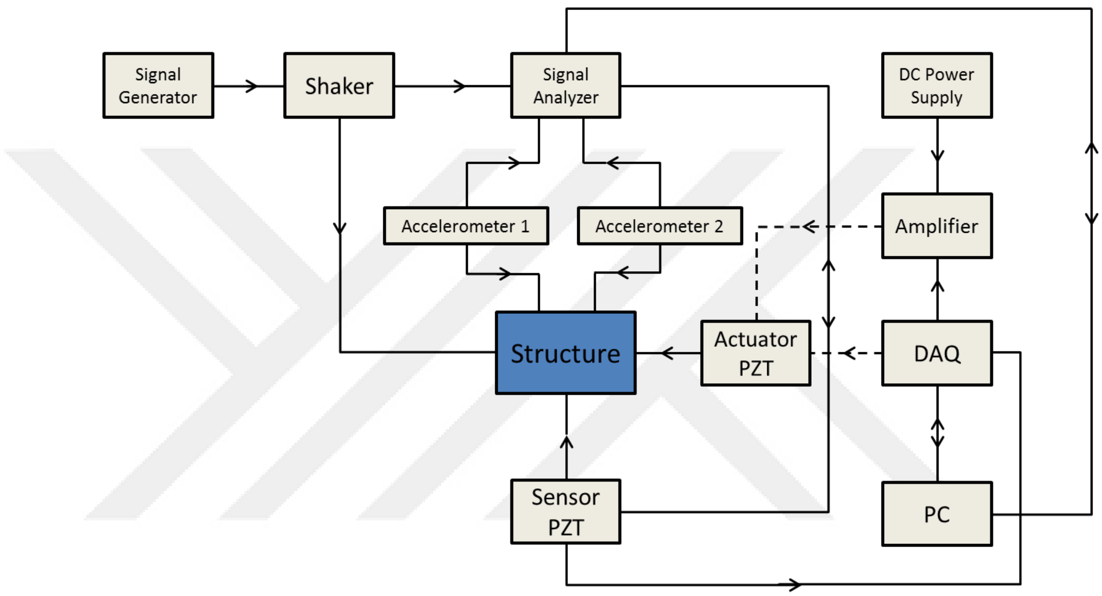

Figure 16 PPF Controller Configuration Diagram

4.3.1 PPF Algorithm

In this study, Positive Position Feedback (PPF), initially proposed by Fanson and Caughey [23], is chosen for vibration suppression. PPF is known to be effective on suppressing single mode vibration of structures [24]. In addition to that, PPF is also acknowledged to control the target vibration mode without destabilizing higher frequency modes of structure [23].

The governing equations for the PPF controller are shown as follows.

$$\begin{aligned} structure&: \ddot{\delta} + 2\zeta\omega\dot{\delta} + \omega^2\delta = g\omega^2\eta \\ compensator&: \ddot{\eta} + 2\zeta_f\omega_f\dot{\eta} + \omega_f^2\eta = \omega_f^2\delta \end{aligned} \tag{5}$$

Here δ is the modal coordinate of the complex panel, η is the filter coordinate, ω and ω_f are the structure and filter frequencies, and ζ and ζ_f are the structural and compensator damping ratios respectively. g is the scalar gain of the controller and greater than 0.

Using Equation (5), the transfer function for the PPF compensator can be written as

$$\boldsymbol{H_f(s)} = \frac{\omega_f^2}{s^2 + 2\zeta_f\omega_f s + \omega_f^2} \tag{6}$$

The basic tuning parameters of the PPF are the natural frequency and the damping ratio ζ_f and gain g of the PPF controller. In this study, since the natural frequency ω_f is adjusted to the vibration mode of interest of the vehicle panel, damping and gain of the controller should be optimized such that the controller suppresses the target frequency effectively.

The block diagram of the PPF controller is given in

Figure **17**. Here d is the disturbance signal on the structure created by the input w. The output signal y is the measured sensor output. The designed PPF controller has the input of the sensor signal y. The output of the controller, u, is then fed to the actuator used for the suppression of the vibration.

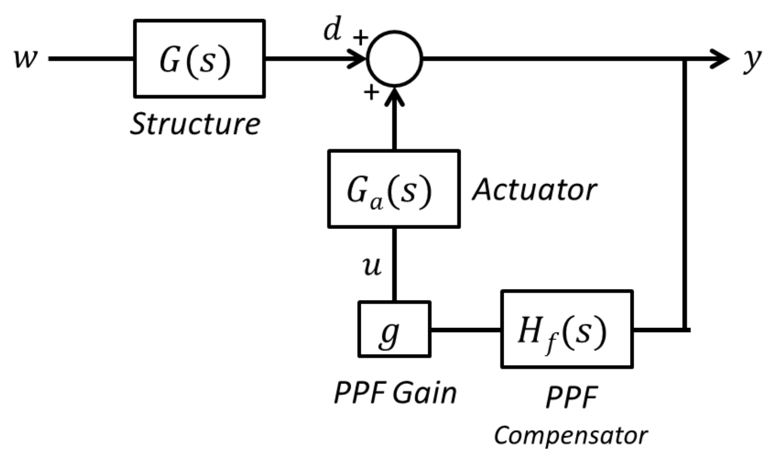

Figure 17 PPF Block Diagram

4.4. Response Surface Methodology

Finding the optimal damping and gain values of PPF controller for various objectives will be based on RSM approach. This approach enables to obtain degree of relationship between multiple factors and output, and also extracts equation for the output as a function of factors. An important part of RSM is the DOE method [25]. These methods were emerged from mathematical model fitting of physical experiments. The purpose of DOE is to include the design factors as combinations and evaluate their outputs. The results of DOE are linked to mathematical models of the experiment. Mostly, these mathematical models are polynomials which are constructed for every particular problem. Therefore, the determination of the factors for the design of experiments has a large influence on the accuracy of the modelling and establishing the response surface.

A comprehensive explanation of the design of experiments and RSM theory are stated in [25] and [26]. Schoofs [27] has reviewed the utilization of DOE for structural optimization, Unal et al. [28] described the use of d-optimal designs for RSM and multidisciplinary design optimization. Simpson et al. [29] presented an overall review about the role of statistics in design.

Response surface methodology is a combination of mathematics and statistics for empirical model extraction. The aim is to optimize a response which is impacted by various independent variables. A series of tests, called runs, are performed in order to track the changes in response and identify the main effects. Consider an optimization problem with two variables,

$$y = f(x_1, x_2) + \varepsilon \tag{7}$$

where ε represents the noise or error observed in response y. The surface represented by $f(x_1, x_2)$ is called a response surface.

Mostly, the degree of the relationship between the response and the independent input variables is not known and a suitable approximation for relationship should be found. Two important models are commonly used in RSM. The first order of the Eq. (7) is,

$$y = \beta_0 + \beta_1 x_1 + \cdots + \beta_k x_k + \varepsilon \tag{8}$$

and the second order is,

$$y = \beta_0 + \sum_{i=1}^{k} \beta_i x_i + \sum_{i=1}^{k} \beta_{ii} x_i^2 + \sum_{i<j} \beta_{ij} x_i x_j + \varepsilon \tag{9}$$

In this thesis, we will deal with the second order equation approximation.

In order to build a quadratic (second order) model, the factors must be varied at 3 levels. A 2^k design with center points is insufficient since second order components are not included in the equation. A 3^k design is possible, but not recommended since the number of runs are higher and some of the runs are unnecessary to fit a quadratic model. Two designs are widely used which find compromise between number of runs and accuracy to fit quadratic models: Central Composite Design and Box-Behnken Design. The preference between these models is based on the practicable number of runs and number of factors. The main differences between these models are described in [25] in detail. Table 3 shows the number of runs required up to 6 factors for Central Composite and Box-Behnken designs. From the table, it is clear that up to 4 factors Box-Behnken design is advantageous in requiring a fewer number of runs. Since the number of factors is 2 (e.g. damping and gain) in this study, Central Composite Design is utilized.

Table 3 Number of Runs and Factors Required by Central Composite and Box-Behnken Designs [25]

Number of Factors	Central Composite	Box-Behnken
2	13 (5 Center Points)	-
3	20 (6 Center Points)	15
4	30 (6 Center Points)	27
5	33 (fractional factorial)	46
6	54 (fractional factorial)	54

4.4.1 Central Composite Design

A second-order model can be constructed efficiently with central composite designs (CCD) [26]. CCD is a composition of first-order designs with additional center and axial points to estimate the tuning parameters of a second-order model. Figure 18 shows a CCD for 2 design variables.

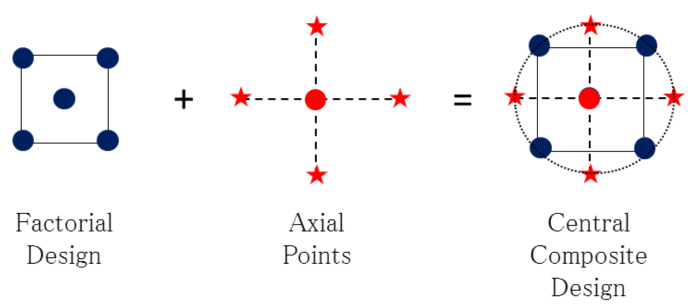

Figure 18 Central Composite Design (CCD) for 2 Variables

In Figure 18, the design involves 2^k factorial points, 2k axial points and 1 central point. The star points represent new values for the low and high settings for all factors. For this reason, CCD is an alternative to General Full Factorial (GFF) especially for 2 variable case since the additional experimental runs are chosen to get more information that yield the optimum. CCD was firstly used by Eschenauer and Mistree [30] for the multi-objective design of a flywheel.

There are three types of CCD: Central Composite Circumscribed (CCC), Central Composite Inscribed (CCI) and Central Composite Face Centered (CCF). CCC design is the basic form of the CCD. The star points are at specific distance, called α from the center based on the number of factors in the design [26]. CCC designs require 5 levels for each factor $(+\alpha, \max, \text{center}, \min, -\alpha)$. When the limits specified for factor settings are the actual experiment limits, the CCC design is useless since additional star points exceed the experiment limits. In this case, CCI or CCF designs should be utilized based on their properties. A CCI design is a scaled down CCC design where the factorial points are brought into the inside of the design space by locating the axial points at the lower and upper bounds of the factor levels. The new points are specified at the same α distance from the center which and are proportional to the axial points. This design also requires 5 levels of each factor. Another type of CCD, CCF design specifies star points at the center of each face, and corresponding $\alpha = \pm 1$. This type of design requires 3 levels of each factor. Figure 19 depicts the schematic representation of three types of CCD.

To make the right selection among CCD alternatives, differences between them should be understood in terms of the experimental region of interest and region of operability [31]. Region of interest is defined as lower and upper limits which are determined by the experimental designer. Region of operability is defined as lower and upper limits which can be operationally achieved with acceptable safety and reasonable outputs [31]. This means that PPF controller parameters should be selected such that the experiments are operated at all time and parameter level setting combinations should be in the region of interest.

As previously stated, extending the axial points beyond the defined variable bounds with CCC designs requires operating the process at five level settings of each variable. However in face-centered CCD (CCF), there are only three level settings of each variable. This makes CCF a simpler design to carry out when the region of operability encompasses the region of interest [31]. Due to insufficient reduction in prediction error and insufficient difference in effects estimation, the benefits of CCC designs do not compensate the added complexity and associated risk. Therefore the CCF is the modest choice for most experiments [26].

For this reason, an initial experimental study is performed on the structure and possible minimum and maximum values of the PPF controller parameters are investigated such that the controller's stability is attained in all configurations. As a result, CCF design is selected in this study since the PPF controller becomes unstable when damping and gain are not within the [0.1, 0.7] and [0.1, 1.4] range respectively. CCF parameter settings for 2 factors are explained below step by step.

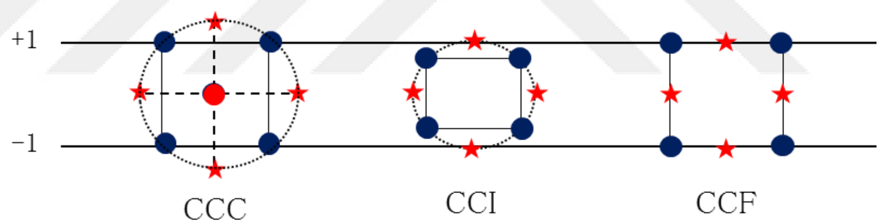

Figure 19 Comparison of Three Types of Central Composite Designs (CCD) for 2 Variables

The steps to follow to construct a CCF design is as follows [32],

1. A complete 2^k factorial design whose factors' levels are coded as min, max. This is called the factorial portion.

2. An axial portion consisting of $2k$ points arranged so that two points are chosen on the axis of each control variable at a distance of $\alpha = 1$ from the design center

3. *5* center points to calculate variance between repeated measurements

The CCF of this study (k = 2, damping and gain) has the form

$$\begin{bmatrix} \mathbf{0.1} & \mathbf{0.1} \\ \mathbf{0.7} & \mathbf{0.1} \\ \mathbf{0.1} & \mathbf{1.4} \\ \mathbf{0.7} & \mathbf{1.4} \\ \mathbf{0.1} & \mathbf{0.75} \\ \mathbf{0.7} & \mathbf{0.75} \\ \mathbf{0.4} & \mathbf{0.1} \\ \mathbf{0.4} & \mathbf{1.4} \\ \mathbf{0.4} & \mathbf{0.75} \\ \mathbf{0.4} & \mathbf{0.75} \\ \mathbf{0.4} & \mathbf{0.75} \\ \mathbf{0.4} & \mathbf{0.75} \\ \mathbf{0.4} & \mathbf{0.75} \end{bmatrix} \tag{10}$$

4.5. Optimal PPF Controller Parameters Investigation

Two metrics are selected for the controller performance as vibration suppression at target frequency and broadband energy reduction (H_2 norm). PPF controller parameters are damping and gain. In the literature, the range of the controller filter damping ratio is usually set between 0.01 and 1 [7]. Closed loop response is directly related to the gain so that the PPF controller performance at the tuned mode increases as the gain increases [33]. Damping and gain values are kept in [0.1, 0.7] and [0.1, 1.4] range respectively as indicated in previous section. Reaching the optimal suppression at the target frequency or achieving broadband energy reduction is separately analyzed. However, both conditions are desired for better performance. For that reason, a multi-objective optimization is also performed to satisfy both conditions. All the results of the single and the multi-objective optimization case studies are presented in the upcoming subsections.

4.5.1 Target Frequency Suppression

The objective is maximum vibration suppression at the target frequency of 143 Hz. To achieve this, the CCF matrix with 13 runs is performed experimentally and the results are analyzed statistically. The number of runs was determined in previous chapter by a complete 2^k factorial points where levels are coded as min and max, 2k axial points which represent the center points of each factor and 5 central points to calculate variance between repeated measurements, which adds up to 13. As an output, the parameters are fitted to the quadratic model and Analysis of Variance (ANOVA) test is applied to test the significance of each parameter. The statistical analysis of these parameters is given in Table 4.

Table 4 Statistical Analysis of Damping and Gain Values for Target Frequency Suppression

Estimated Regression Coefficients for Target Frequency Suppression

Term	***Coef***	***SE Coef***	***T***	***P***
Constant	6.64412	0.01182	562.194	0.000
Damping	-0.02000	0.01258	-1.59	0.151
Gain	4.68167	0.01258	372,109	0.000
Damping*Damping	-0.04647	0.01831	-2.538	0.035
Gain*Gain	-1.80147	0.01831	-98.394	0.000
Damping*Gain	0.03500	0.01541	2.271	0.053

S = 0.0308181 PRESS = 0.0737108
R-Sq = 99.97% R-Sq(pred) = 99.95% R-Sq(adj) = 99.99%

The significance of each coefficient is evaluated by examining T and P values. T value corresponds to division of ‘Coef’ by ‘SE Coef’. High T and small P (≤ 0.05) is required to be a significant coefficient. In this case, linear effect of damping is less significant while the remaining linear and quadratic effects are more significant. R-Squared (R-Sq) value of

99.97 % shows how close the data are to the fitted regression line. From the results of the RSM, the estimation equation and the response surface plot is shown in Figure 20.

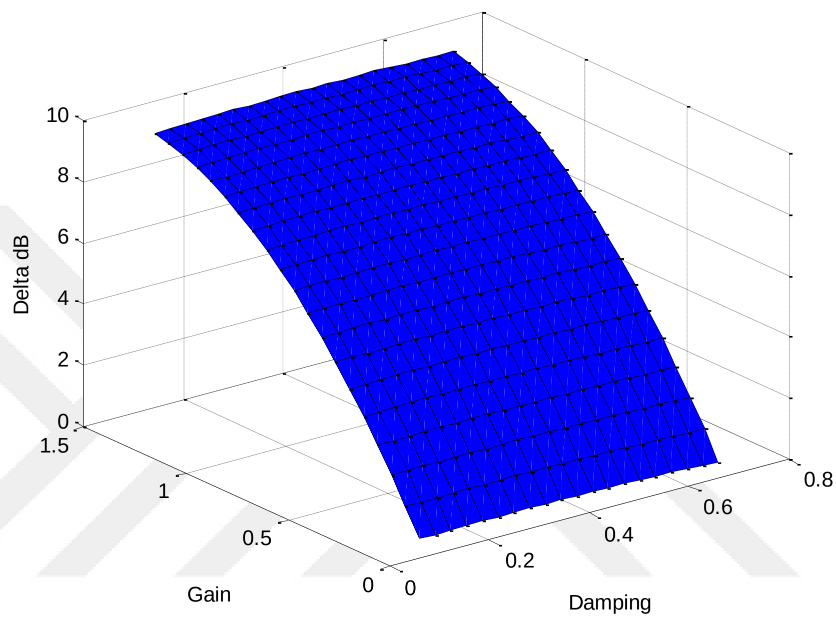

$$\Delta dB = -1.204 + 0.491 * Damping + 13.64 * Gain - 0.865 * Damping^2 - 4.338 * Gain^2 + 0.179 * Damping * Gain$$

Figure 20 Surface Plot of Target Frequency Suppression and the Quadratic Model

By analyzing the data, the effectiveness of PPF at the target frequency due to the gain value is high. As gain is increased, amount of suppression increases and best performance is obtained by maximum gain value. On the other hand, the effectiveness of the PPF at the target frequency was only slightly reduced when changing damping ratio from 0.1 to 0.7. These results are in agreement with the literature [34]. Even a slight change occurs, optimization algorithm recommends a nearly center value, 0.4273 for damping, and 1.4 for gain. With this configuration, maximum of 9.55 dB reduction is achieved at 143 Hz as illustrated in Table 6.

4.5.2 Broadband Energy Reduction by H_2 Norm

Another topic that the authors have been considering about the effectiveness of the PPF controller is the broadband energy reduction based on H_2 norm since the minimization of the closed loop response at a single frequency can yield the augmentation of the vibration energy at other frequencies. H_2 norms of the closed loop and open loop frequency responses are calculated and the difference between them is used as an optimization metric. Firstly, the H_2 norm is calculated as below,

$$E = \left(\frac{1}{2\pi} \int_{w_0}^{w_1} |H(jw)|^2 dw \right)^{1/2} \tag{11}$$

$$\Delta E = \frac{E_{CL} - E_{OL}}{E_{OL}} \tag{12}$$

where $w_0 = 20\,Hz$ and $w_1 = 312\,Hz$, and E is the value of H_2 norm. By taking difference of the open and closed loop norms and dividing with the open loop value, energy reduction for each point is calculated between w_0 and w_1. To optimize the PPF controller parameters in this section, the same runs from the previous section has been performed and the results are collected in terms of H_2 norm energy difference and the results are analyzed statistically. As an output, the parameters are fitted to the quadratic model and Analysis of Variance (ANOVA) test is applied to test the significance in each parameter. The statistical analysis of these parameters is given in Table 5.

Table 5 Statistical Analysis of Damping and Gain Values for Energy Reduction Based on H_2 Norm

Estimated Regression Coefficients for Energy

Term	***Coef***	***SE Coef***	***T***	***P***
Constant	-23.729	0.2485	-95.477	0.000
Damping	-2.229	0.2444	-9.121	0.000
Gain	-12.539	0.2444	-51.316	0.000
Damping*Damping	1.337	0.3602	3.712	0.008
Gain*Gain	4.313	0.3602	11.974	0.000
Damping*Gain	-1.330	0.2993	-4.443	0.003

S = 0.598540 PRESS = 19.5727
R-Sq = 99.76% R-Sq(pred) = 98.16% R-Sq(adj) = 99.60%

The significance of each coefficient is evaluated by examining T and P values as in previous section. In this case, all linear and quadratic effects are significant. R-Sq value of 99.76 % shows how close the data are to the fitted regression line. From the results of the RSM, the estimation equation and the response surface plot is shown in Figure 21.

By analyzing the data, the effectiveness of PPF in terms of H_2 norm due to the gain value is high. As you increase gain, the amount of energy reduction increases and the best performance is obtained by maximum gain value. On the other hand, the effectiveness of the PPF due to damping value is also significant. Maximum value of damping is required for maximum energy reduction based on H_2 norm. These results are in agreement with the literature [34]. Optimization algorithm recommends a maximum value for both damping and gain, which are 0.7 and 1.4 respectively. With this configuration, maximum energy reduction we can achieve is 34.17% for the overall frequency range.

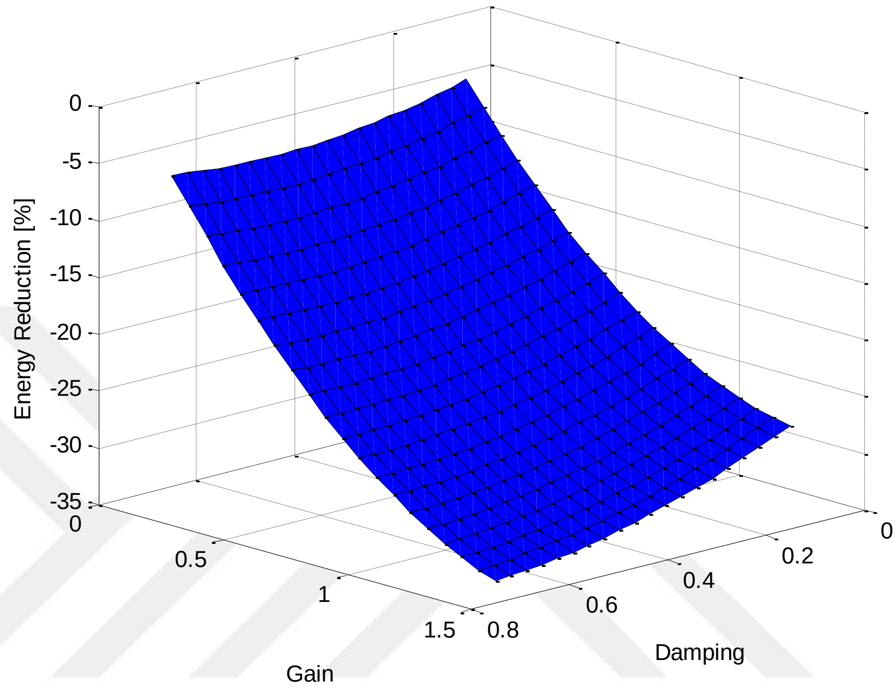

$$\Delta E = -0.217 - 14.197 * Damping - 31.874 * Gain + 14.853 * Damping^2 + 10.207 * Gain^2 - 6.819 * Damping * Gain$$

Figure 21 Surface Plot of Energy Reduction Based on H_2 Norm and the Quadratic Model

4.5.3 Multi-Objective Optimization

The optimal values for one of the responses probably will not be the optimal values for some other response, where we need multi objective optimization. There are several techniques to optimize multi response problems such as finding the Pareto optimal result, exist [35]. In this thesis, two different techniques are used for multi-objective optimizations which are weighted sum approach and D-optimality approach. Then the results are compared.

4.5.3.1. Weighted Sum Approach

The approach to minimize the weighted sum of the normalized objectives defined as:

$$f_{ws} = \sum_{n=1}^{m} w_n \overline{f_n} \tag{13}$$

where $\overline{f_n}$ are normalized objective functions and w_n are corresponding weights. With this approach, optimization of all responses simultaneously is possible by combining them into a single objective function such that values lie in the range [0,1] [36]. Other than normalization, a weight is assigned to each objective depending on their importance for the design. If the weights are selected at which their sum is equal to 1.0, it is ensured that the magnitude of the combined objective $|f_{ws}|$ is also in the range [0,1]. Usage of different weights changes the optimum in general. It should also be noted, if one weight is selected as 0.0, the problem reduces to a single-objective problem.

The responses were optimized individually in previous sections. Maximum value of vibration suppression at the target frequency was 9.55 dB. In this setting, gain is at maximum level and damping is 0.4273. Maximization of energy reduction based on H_2 norm has resulted in %34.17. In latter case, factors damping and gain were at their maximum level.

The multi objective optimization is performed through the normalized weighted sum of target frequency suppression (TFS) and H_2 norm energy reduction (ER), as shown in Figure 22. An equal weight (i.e. $w_{TFS} = 0.5$ and $w_{ER} = 0.5$) is used for target frequency suppression and H_2 norm energy reduction cases. As Figure 22 indicates, the optimum point location for multi objective case lies at a location where damping = 0.7 and gain = 1.4. Remember, this is the same as optimum of H_2 norm energy reduction single objective case. This result demonstrates the fact that damping is not so significant in the selected metrics. One may investigate the optimal configuration by repeating the calculations for different weights (i.e. $w_{TFS} = 0.85$ and $w_{ER} = 0.15$) such that other design configurations can be obtained.

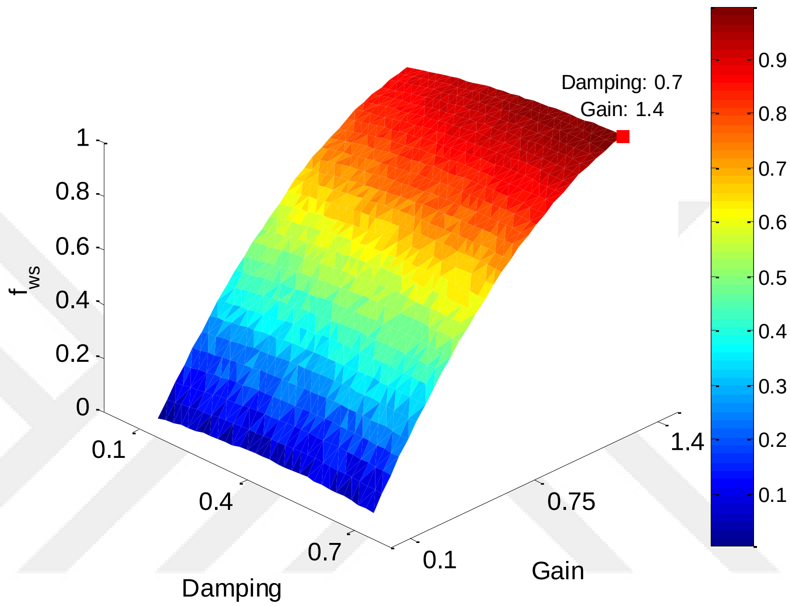

Figure 22 The Normalized Weighted Sum of Target Frequency Suppression and H_2 Norm Energy Reduction for the Weights $w_{TFS} = 0.5$ and $w_{ER} = 0.5$

For the optimal condition, frequency suppression at target frequency becomes 9.48 dB and energy difference based on H_2 norm is 34.17%. This observation recommends using higher damping values in the PPF controller design to achieve multi-objective optimization since effectiveness at the targeted mode will not be much effected by a higher damping value. The overall configuration and results are illustrated in Table 6.

Table 6 Optimization Results

Single Objective Case

Response	***Damping***	***Gain***	***Result***
dB Reduction	0.4273	1.4	9.55
H_2 Norm	0.7	1.4	34.17

Multi Objective Case

Response	***Objective***	***Damping***	***Gain***	***Weight***	***Result***
dB Reduction	Maximize	0.7	1.4	0.5	9.48
H_2 Norm	Maximize			0.5	34.17

4.5.3.2. D-Optimality Approach

Another method to solve multi-objective optimization problems is the d-optimality approach. In this method, optimization of all responses simultaneously is possible by combining them into a single objective function which basically represents the relationship of all responses that are to be optimized [35].

The desirability function is a conversion of the response variable to a 0 to 1 scale. This method identifies operating conditions that provide the "most desirable" response values or output of an experiment. A desirability function response of 0 is an absolutely undesirable response where response of 1 is the most desirable. In order to optimize several responses simultaneously, geometric means of each desirability responses are combined to create the overall desirability. The mathematical formulation of overall desirability function, $D(Y)$ with several responses is defined as,

$$D(Y) = \sqrt[n]{d_1(y_1)^{k_1} \times d_2(y_2)^{k_2} \times d_3(y_3)^{k_3} \times \ldots \times d_n(y_n)^{k_n}} \tag{14}$$

where y_i denote the value of response i, $d_i(y_i)$ is the converted desirability value of i'th response and k_i represent the relative importance of response i compared to others [37]. If all responses are equally important, overall desirability $D(Y)$ is a geometric mean of all n responses with no weighting. Overall desirability value will be close to 1 if all of the responses are close to their optimal values, and vice versa. As a result, in order to find the optimal, each parameter values should be specified in a way to maximize $D(Y)$.

Different desirability functions are used depending on whether a particular response is minimized, maximized or assigned a target value [38]. In this thesis, there is one type of desirability function since aim is to maximize both vibration suppression at target frequency and the H_2 norm energy reduction. The individual desirability function for response maximization is defined as [38]

$$d_i(y_i) = \begin{cases} 0 & y_i < L_i \\ \left(\dfrac{y_i - L_i}{U_i - L_i}\right)^s & L_i < y_i < U_i \\ 1 & y_i > U_i \end{cases} \tag{15}$$

Here, L_i, T_i and U_i are the lower limit, upper limit and target values, respectively. And the desired response Y_i is defined in the region of $L_i \leq T_i \leq U_i$. s specifies the weight exponent in the range of interest. For s=1 the desirability function increases linearly towards T_i, for s>1 the function is convex, and for s>1 the function is concave, as in [35].

As previously stated, the desirability approach converts multiple objectives in a single objective called D. Therefore the aim now is to maximize the overall desirability value. This is achieved by direct search methods [39]. The estimated responses and the individual desirabilities $d_i(y_i)$ of the estimated responses are continuous functions of the factors (e.g. damping and gain). Thus, the overall desirability function, $D(Y)$ is a continuous function of the factors. After all factor levels are searched, an optimal point that maximizes the overall desirability is found by a direct search method. This method gives rather good convergence results.

The responses were optimized individually in previous sections. Maximum value of vibration suppression at target frequency was 9.55. In this setting, gain is at maximum level and damping is 0.4273. Maximization of energy reduction based on H_2 norm has resulted in %34.17. In this case, factors damping and gain were at their maximum level.

The multi-objective optimization calculations by d-optimality approach are performed through MINITAB software. Maximum value of overall desirability function for these two responses obtained is 0.938. For the optimal condition, frequency suppression at target frequency becomes 9.48 and broadband energy reduction based on H_2 norm is 34.17. This observation recommends using higher damping values in the PPF controller design to achieve multi-objective optimization since effectiveness at the targeted mode will not be much effected by a higher damping value. The overall configuration and results are illustrated in Table 7. By examining Table 6 and Table 7, one can state that both approaches (e.g. weighted sum and d-optimality) recommend the same factor levels and output the same result.

Table 7 D-Optimality, Multi-Objective Optimization Results

Response	***Objective***	***L_i***	***T_i***	***Result***	***d_i***	***D***
H_2 Norm	Maximize	30	34.17	34.17	0.977	0.938
dB Reduction	Maximize	9	9.55	9.48	0.90	

4.6. Experimental Verification of Optimization Studies

In this section, optimization results are verified experimentally. To achieve this, the experimental setup explained in section 4.2 and 4.3 is utilized. The optimal configuration offered by the quadratic model is implemented as input to the PPF controller and the results are compared. Table 8 shows a good agreement between the experimental and numerical results. Target frequency vibration suppression metric is shown as Case 1 and H_2 norm energy reduction as Case 2. Note that, in single objective cases, the optimal value was obtained when damping value was 0.4273 and gain was 1.4 in Case 1. In Case 2, the optimal value was obtained when damping was 0.7 and the gain was 1.4. The multi-objective optimization results are illustrated on the right hand side of Table 8. For multi objective case, the optimal setting for damping and gain values were 0.7 and 1.4, respectively.

Table 8 Experimental Verification Results of Single and Multi-Objective Cases

	Single Objective		Multi-Objective	
	Estimated	Experimental	Estimated	Experimental
Case 1 [dB]	9.55	9.56	9.48	9.49
Case 2 [%]	34.17	34.11	34.17	34.11

Chapter 5

DEMONSTRATION OF PPF CONTROLLER PERFORMANCE ON A VEHICLE

5.1. Overview

In this section, the same AVC approach is extended to a real vehicle and the results are obtained when the vehicle is in the operating conditions. A stand-alone controller configuration with low power consumption is developed in combination with a signal conditioner unit. The developed configuration is suitable for the vehicle applications in operating conditions and can be powered by the electrical supply available in the vehicle. The test vehicle, road type and measurement locations are indicated in Figure 23.

Figure 23 Test Vehicle, Selected Road Profile and Measurement Locations

5.2. Vehicle Instrumentation

Vehicle implementation of the proposed AVC requires developing proper instrumentation that would not exceed the vehicle's maximum allowable voltage and current. The maximum allowable voltage of the vehicle is 12V where 19.5V and 24V are required for the PC and the amplifier, respectively. The required equipment for on-vehicle studies are: ADVANTECH ARK 3500P industrial PC, TFT-LCD type screen, 12V to 24V power invertor, 1 car DC outlet (cigarette lighter) multiplexor, 2 P876.A12 piezoelectric patches, 1 PZT amplifier and NI-PCI 6229 connector. For the proposed configuration, total current is 4.75A, and total power requirement is 60W where maximum allowable current and power limit are 15A and 180W, respectively. The ground supply to PZT amplifier is from the chassis. The working diagram of this configuration is illustrated in Figure 24.

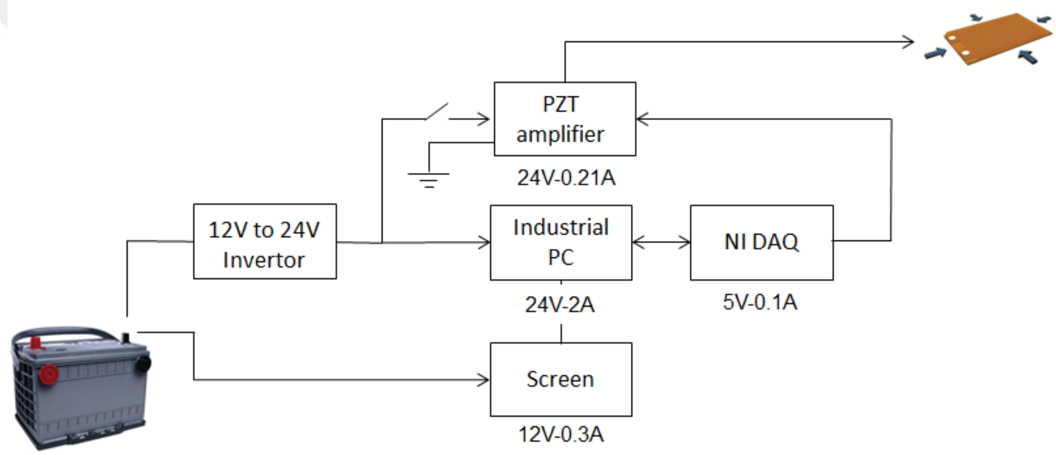

Figure 24 Working Diagram of On Vehicle AVC Configuration

ADVANTECH ARK 3500P is an industrial computer with its compact casing which enables easy handling and low power consumption while performing the tests. TFT-LCD type screen is for monitoring the output data. 12V to 24V power invertor is used to increase 12V input from the battery to 24 V which is necessary for PC and PZT amplifier. Two P876.A12 piezoelectric patches and one PZT amplifier are used for controller purposes where NI-PCI 6229 DAQ card is necessary to embed the controller PPF algorithm and send actuator signal to PZT actuator. The details of the on vehicle configuration are shown in Figure 25.

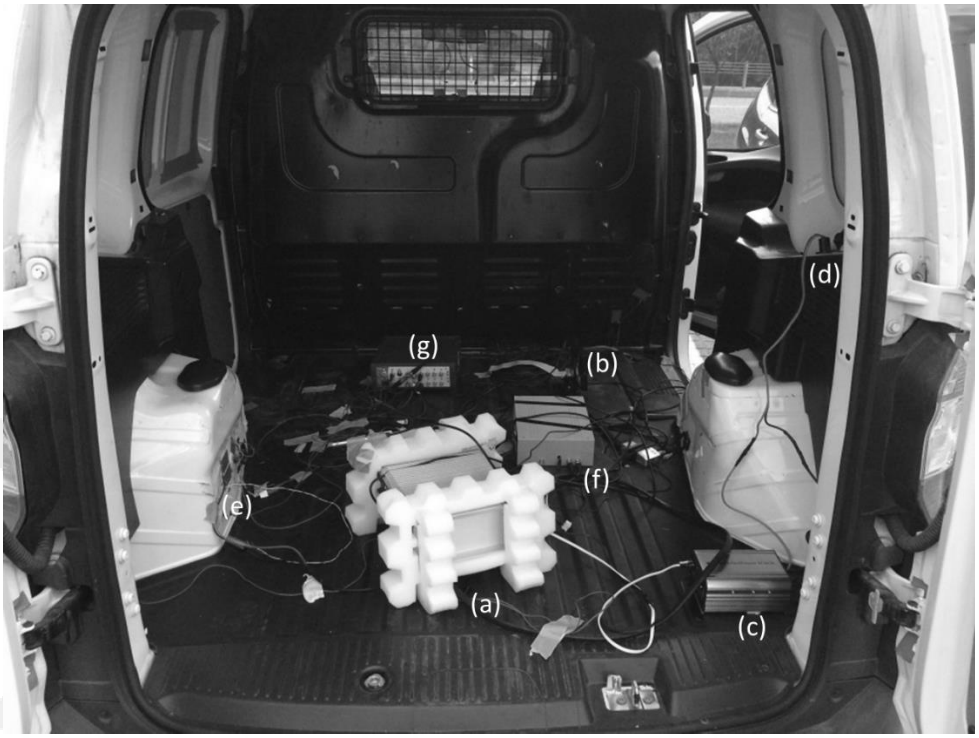

Figure 25 Details of the running vehicle experimental set-up a) Industrial PC b) TFT LCD Screen c) Power Invertor d) DC Outlet Multiplexor e) Piezoelectric Patches f) PZT Amplifier g) Signal Analyzer

5.3. AVC Experimental Results on Vehicle

A modal test is repeated on the wheelhouse to see the effect of the other components of the vehicle and the real boundary conditions on the wheelhouse dynamics. This step is required to determine the controller and filter natural frequency, ω and ω_f. Since the wheelhouse mode shape is well known from the previous studies in the laboratory environment, the region of interest on the wheelhouse is reduced and the modal test is performed with 7 accelerometer locations. The first three modes are 152.3 Hz, 204.7 Hz and 222.7 Hz. Actuator and sensor patch locations are kept the same as laboratory studies.

In the quarter BIW assembly, the problematic mode was 143 Hz whereas on vehicle, it shifts to 152.3 Hz. This could be due to the additional components and boundary conditions of the real vehicle. The additional components are damping materials and protective layers as well as the additional substructures such as fuel line and tire assembly on the outer side of the wheelhouse. Additionally, this deviation may be due to quarter BIW assembly being cut from a Kombi buck and test vehicle is Van type. And of course a minor frequency difference is expected between system level and vehicle level wheelhouse panel.

The road tests were performed with constant speed of 60 km/h at 2000 rpm in the 3rd gear. Two accelerometers were placed on the wheelhouse panel to monitor the behaviour on other locations and one sensor patch was used to collect the vibration attenuation data on each run. Five replicated runs were performed at the same paths which enables driving the vehicle for 30 seconds with the same operational conditions. Both open loop and closed loop data were analysed to see the variations between and within each run. To statistically prove that the results are reliable, calculated probability, p values and standard deviations are shown in Table 9. Since p values are more than 0.05 and maximum standard deviation is found to be 2.73, it is clear that the closed loop data have a normal distribution with reasonable standard deviations. So, variation of acceleration values in each measurement cycle is stable.

Table 9 Statistical Analysis of Vehicle Level Results

	PZT Sensor		Accelerometer 1		Accelerometer 2	
	Closed Loop	Open Loop	Closed Loop	Open Loop	Closed Loop	Open Loop
Mean	99.862	91.265	101.796	108.346	88.235	81.083
St Dev	2.5328	2.7632	2.6383	2.8504	2.7187	2.5755
p value	0.932	0.311	0.932	0.311	0.079	0.12

The closed loop results are evaluated for the PZT sensor and two different accelerometer locations and vibration amğlitude results are illustrated in below plots, respectively. Results indicate that 150 Hz mode of the wheelhouse is suppressed successfully with the controller. Additionally, there is no increase of vibration levels in other measurement locations, which states that AVC algorithm does not amplify other modes of the structure. Closed loop suppression levels show that there are considerable reductions in vibration amplitudes as 8.3 dB, 7.9 dB and 8.1 dB for PZT sensor, accelerometer 1 and accelerometer 2, respectively. Summary of the results are illustrated in

Table **10**.

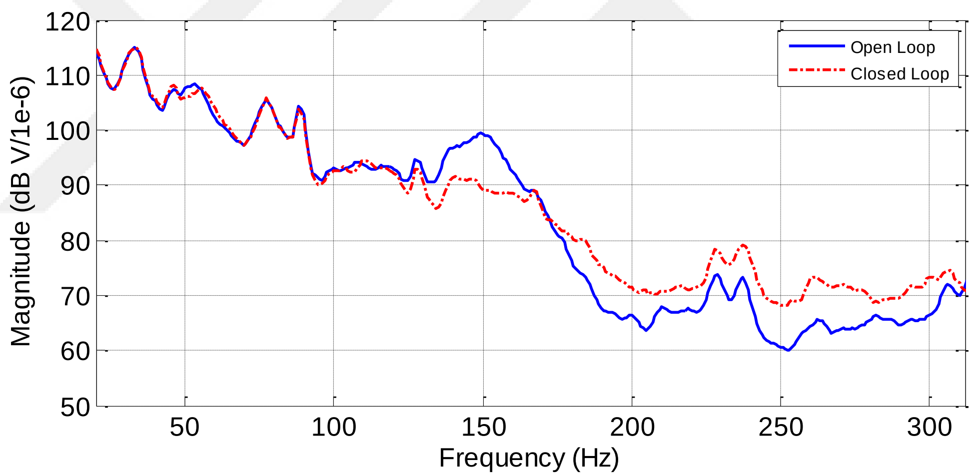

Figure 26 On Vehicle Vibration Level Measurement Results – PZT Sensor

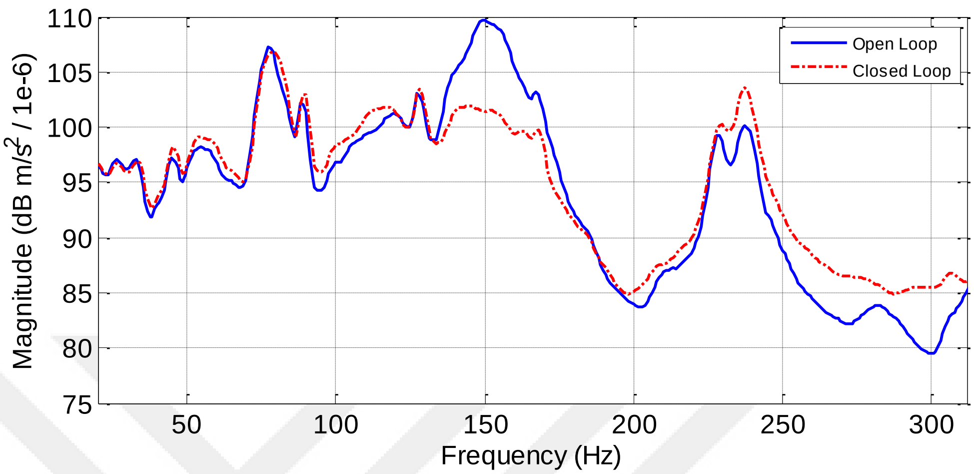

Figure 27 On Vehicle Vibration Level Measurement Results – Accelerometer 1

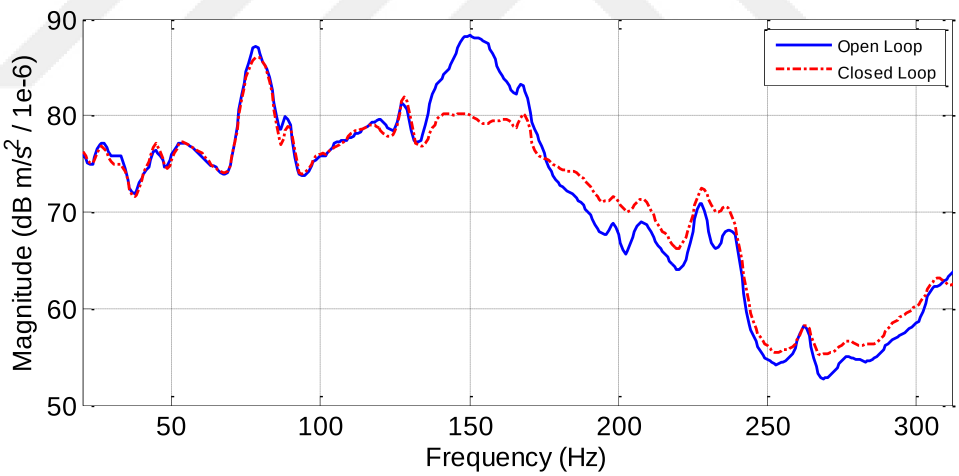

Figure 28 On Vehicle Vibration Level Measurement Results – Accelerometer 2

Table 10 Vehicle Level Vibration Suppression Performances of the PPF Controller for the Sensor Locations

Sensor Type	***Target Frequency Suppression***	***H_2 Norm Energy Reduction***
PZT Sensor	8.3 dB	- 21.87 %
Accelerometer 1	7.9 dB	- 17.48 %
Accelerometer 2	8.1 dB	- 19.63 %

Chapter 6

SUMMARY AND CONCLUSIONS

Among several vibration control mechanisms, piezoelectric sensors and actuators are preferred by researches due to their simplified usage and low weight compared to passive treatments. However, the closed loop performance of the controller still depends on the efficient placement of sensor/actuators and fine tuning of the controller parameters. Considering the needs in vibration control, this thesis presents a methodology which combines numerical and experimental techniques to determine optimum location of piezoelectric patches and optimum controller parameters for AVC for complex structures.

Considering the difficulties encountered in designing a controller as described in the previous studies, a numerical and experimental methodology is developed in this thesis to implement AVC for complex structures.

First the developed methodology is demonstrated on a representative vehicle model in the laboratory environment using a quarter BIW vehicle structure. Optimum location for the sensor/actuator pair is determined numerically by using a validated finite element model of the complex structure. Once the location is determined, the controller parameters (e.g. damping and gain) are varied based on the Design of Experiments (DOE) technique to search for the optimum parameter configuration in the design space. All the DOE configurations are performed experimentally to include the hardware and controller limitations in the analysis. RSM technique is utilized for identifying the relationship between the design parameters and the controller performance. Then, vibration suppression performance is evaluated based on two control metrics, amplitude reduction at the targeted frequency and broadband energy reduction. Single and multi-objective optimization case studies are performed using the above metrics. Finally, the same approach is extended to a real vehicle with hardware modifications due to the power constraints in the operating conditions.

In Chapter 1, importance of vibration control in automotive industry was highlighted and the active vibration control literature was reviewed. The use of piezo-electric materials and PPF control implementations in vibration control were also reviewed and major studies in that area were described

In Chapter 2, the experimental setup used in AVC studies was introduced and FE model was described in detail. The modal test results on the experimental setup were given and the correlation studies were described. The correlation studies included comparing the numerical model results with the experimental ones based on natural frequencies, FRFs calculated between various input and output locations and MAC number method. Maximum error between experimental and numerical results in terms of natural frequency was %1.6. FRF comparison plots indicated that experimental and numerical transfer functions were matching very well. As the final step of correlation, MAC number method showed that the experimentally calculated modes were highly correlated.

In Chapter 3, FE model of the complex structure was integrated with the piezoelectric patches and it was used to determine the optimum piezoelectric patch locations. Details of the FE modelling of the piezoelectric patches were discussed in detail and the mathematical expressions to simulate the piezoelectric behavior were provided. Possible configurations for all possible sensor/actuator locations and orientations were introduced. The performance of each location was evaluated by assessing the transfer functions between the actuator patch and the sensor patch and the best location was selected.

In Chapter 4, PPF controller parameters were determined experimentally by utilizing CCF design of RSM approach in the stable region of the controller. The selection of the CCF design was justified and required number of runs to extract the quadratic model was given. Two performance metrics were selected for searching the optimal PPF controller parameters: highest suppression at the target frequency and H_2 norm energy reduction. The results were analyzed statistically and each metric resulted different damping values but the maximum gain value. Optimization outputs indicated that gain value was the most effective parameter in vibration suppression and energy reduction. Then, multi-objective optimization was performed with different approaches as Weighted Sum and D-Optimality. Both approaches output the same result and optimal parameter configuration was determined as damping = 0.7 and gain = 1.4. With this configuration, 9.48 dB vibration reduction at target frequency and %34.17 energy reduction at broadband was achieved. Then the results were verified experimentally and it is observed that experimental and numerical results were in good agreement.

In Chapter 5, AVC approach was extended to a real vehicle. The developed configuration for vehicle application in operating conditions was discussed in detail. Three measurement points were selected to assess the performance of the controller as one piezoelectric sensor for closed loop performance and two accelerometers to monitor if vibration was increased at other locations. Vehicle level results indicated that active vibration control for automotive applications is promising.

The preliminary results show that the developed methodologies may provide lighter and smarter way for automotive manufacturers to solve vibration problems on automotive panels. The developed methodologies are demonstrated for a commercial vehicle however they are applicable to any complex panels used in other applications.

For future studies, the developed methodology in this thesis can be extended to seek for better vibration suppression performance by utilizing other controller algorithms such as

Linear Quadratic Regulator (LQR), Filtered-X Least Mean Squares (FX-LMS), optimal velocity feedback and so on. Also, other optimization algorithms with higher sampling may be utilized to find optimal PPF controller parameters with higher precision. In addition, the applicability of the proposed technology to real vehicle raises questions about the cost and feasibility. The vehicle level study completed herein involves operation of piezoelectric patches from external computers. For future studies, integration of this system into vehicle's electronic control unit (ECU) should be considered. Other piezoelectric patches can be utilized and explored in AVC applications where operating conditions, vulnerability to moisture and heat, and cabling requirements are also taken into consideration.

BIBLIOGRAPHY

1. Alkhatib, R. and M. Golnaraghi, *Active structural vibration control: a review*. Shock and Vibration Digest, 2003. **35**(5): p. 367.
2. Ro, J. and A. Baz, *Control of sound radiation from a plate into an acoustic cavity using active constrained layer damping*. Smart Materials and Structures, 1999. **8**(3): p. 292.
3. Bailey, T. and J.E. Hubbard, *Distributed piezoelectric polymer active vibration control of a cantilever beam*. Journal of Guidance Control and Dynamics, 1985. **8**(5): p. 605-611.
4. Boz, U., U. Aridogan, and I. Basdogan, *A numerical and experimental study of optimal velocity feedback control for vibration suppression of a plate-like structure*. Journal of Low Frequency Noise, Vibration and Active Control, 2015. **34**(3): p. 343-359.
5. Li, S., et al., *Piezoelectric vibration control for all-clamped panel using DOB-based optimal control*. Mechatronics, 2011. **21**(7): p. 1213-1221.
6. Goh, C. and T. Caughey, *On the stability problem caused by finite actuator dynamics in the collocated control of large space structures*. International Journal of Control, 1985. **41**(3): p. 787-802.
7. Fenik, Š. and L. Starek, *Optimal PPF controller for multimodal vibration suppression*. Engineering Mechanics, 2008. **15**(3): p. 153-173.
8. Fanson, J. and T.K. Caughey, *Positive position feedback control for large space structures*. AIAA journal, 1990. **28**(4): p. 717-724.
9. Crawley, E.F. and J. De Luis, *Use of piezoelectric actuators as elements of intelligent structures*. AIAA journal, 1987. **25**(10): p. 1373-1385.
10. Bruant, I., L. Gallimard, and S. Nikoukar, *Optimal piezoelectric actuator and sensor location for active vibration control, using genetic algorithm*. Journal of Sound and Vibration, 2010. **329**(10): p. 1615-1635.
11. Han, J.-H. and I. Lee, *Optimal placement of piezoelectric sensors and actuators for vibration control of a composite plate using genetic algorithms*. Smart Materials and Structures, 1999. **8**(2): p. 257.
12. Gupta, V., M. Sharma, and N. Thakur, *Optimization criteria for optimal placement of piezoelectric sensors and actuators on a smart structure: a technical review*. Journal of Intelligent Material Systems and Structures, 2010. **21**(12): p. 1227-1243.

13. Liu, X. and J. Hu, *Low order vibration control for structures with highly correlated close modes.* Science China Technological Sciences, 2011. **54**(7): p. 1855-1864.
14. Goh, C. and T. Lee, *Adaptive modal parameters identification for collocated position feedback vibration control.* International Journal of Control, 1991. **53**(3): p. 597-617.
15. Ryan, R.O. and S. Jinjun, *Experimental study on active vibration control using genetic algorithm-based system identification and optimized positive position feedback.* Smart Materials and Structures, 2012. **21**(12): p. 125014.
16. McEver, M.A., *Optimal vibration suppression using on-line pole/zero identification.* 1999.
17. Hibbett, Karlsson, and Sorensen, *ABAQUS/standard: User's Manual*. Vol. 1. 1998: Hibbitt, Karlsson & Sorensen.
18. Ewins, D.J., *Modal testing: theory and practice*. Vol. 15. 1984: Research studies press Letchworth.
19. Aridogan, U., I. Basdogan, and A. Erturk, *Analytical modeling and experimental validation of a structurally integrated piezoelectric energy harvester on a thin plate.* Smart Materials and Structures, 2014. **23**(4): p. 045039.
20. Chin, L., V. Varadan, and V. Varadan. *Finite element methods for numerical simulation of the actuator performance of a composite transducer array*. in *Proc. 1991 Int. Symp. on Active Materials and Adaptive Structures*. 1991.
21. Jeng, J., et al. *A complete finite element-eigenmode analysis for a 1-3 type of piezoelectric composite transducer including the effect of fluid loading and internal losses*. in *Ultrasonics Symposium, 1988. Proceedings., IEEE 1988*. 1988. IEEE.
22. Kim, J.-W., V.V. Varadan, and V.K. Varadan. *Finite element modeling of a finite piezoelectric sensor/actuator embedded in a fluid-loaded plate*. in *1994 North American Conference on Smart Structures and Materials*. 1994. International Society for Optics and Photonics.
23. Fanson, J.L. and T.K. Caughey, *Positive position feedback control for large space structures.* AIAA Journal, 1990. **28**(4): p. 717-724.
24. Ratnam, M., et al. *PPF Control of a Piezoelectric Tube Scanner*. in *Decision and Control, 2005 and 2005 European Control Conference. CDC-ECC '05. 44th IEEE Conference on*. 2005.
25. Box, G.E. and N.R. Draper, *Empirical model-building and response surfaces*. Vol. 424. 1987: Wiley New York.
26. Montgomery, D.C., *Design and analysis of experiments*. 2008: John Wiley & Sons.
27. Schoofs, A.J.G., *Experimental design and structural optimization*. 1988: Springer.
28. Unal, R., D.O. Stanley, and R.A. Lepsch, *Parametric modeling using saturated experimental designs.* Journal of Parametrics, 1996. **16**(1): p. 3-18.

29. Simpson, T.W., et al., *On the use of statistics in design and the implications for deterministic computer experiments.* Design Theory and Methodology-DTM'97, 1997: p. 14-17.
30. Lautenschlager, U., H.A. Eschenauer, and F. Mistree, *Multiobjective flywheel design: a doe-based concept exploration task.* Advances in Design Automation (Dutta, D., ed.), 1997: p. 14-17.
31. Verseput, R., *Digging into DOE Selecting the right central composite design for response surface methodology applications.* Quality Digest, 2001. **21**(6): p. 33-36.
32. Khuri, A.I. and S. Mukhopadhyay, *Response surface methodology.* Wiley Interdisciplinary Reviews: Computational Statistics, 2010. **2**(2): p. 128-149.
33. Shin, C., C. Hong, and W.B. Jeong, *Active vibration control of clamped beams using positive position feedback controllers with moment pair.* Journal of mechanical science and technology, 2012. **26**(3): p. 731-740.
34. Song, G., S.P. Schmidt, and B.N. Agrawal. *Experimental study of active vibration suppression of flexible structure using modular control patch*. in *Aerospace Conference, 1998 IEEE*. 1998. IEEE.
35. Aksezer, S.Ç., *On the sensitivity of desirability functions for multiresponse optimization.* 2008.
36. Serhat, G., T.G. Faria, and I. Basdogan, *Multi-Objective Optimization of Stiffened, Fiber-Reinforced Composite Fuselages for Mechanical and Vibro-Acoustic Requirements.* 2016.
37. Akçay, H. and A.S. Anagün, *Multi Response Optimization Application on A Manufacturing Factory*. Mathematical and Computational Applications, 2013. **18**(3): p. 531-538.
38. Derringer, G. and R. Suich, *Simultaneous optimization of several response variables.* Journal of quality technology, 1980. **12**(4): p. 214-219.
39. Lewis, R.M., V. Torczon, and M.W. Trosset, *Direct search methods: then and now*. Journal of computational and Applied Mathematics, 2000. **124**(1): p. 191-207.